LA-UR-23-30155

Approved for public release; distribution is unlimited.

Title: Diffusional creep in UO2 informed by lower length scale simulations

Author(s): Galvin, Conor Oscar
Andersson, Anders David Ragnar
Sweet, Ryan
Capolungo, Laurent
Cooper, Michael William Donald

Intended for: Report

Issued: 2024-02-26 (rev.1)

Los Alamos
NATIONAL LABORATORY

Diffusional creep in UO_2 informed by lower length scale simulations

C. O. T. Galvin[a], D. A. Andersson[a], R. Sweet[b], L. Capolungo[a], and M. W. D. Cooper[a]

[a]*Materials Science and Technology Division, Los Alamos National Laboratory*
[b]*Idaho National Laboratory, 1955 N Fremont Ave, Idaho Falls, ID 83415, USA*

August 31st, 2023

Executive Summary

Using molecular dynamics, we predict information at the atomistic scale used to develop a mechanistic UO_2 creep model for use in higher length-scale fuel performance codes. The ultimate objective of the model is to not only to capture the creep rates of UO_2 but to determine the dominant mechanism in the diffusional regime, which is still debated in the literature. It is important to have a model to capture the correct mechanisms for creep in UO_2 as this can be used as the foundation when applying to other fuels, such as doped UO_2, and when irradiation is accounted. In last years NEAMS milestone (FY22), we developed a prelimnary model, however there were issues, for example, excessively high values of uranium vacancy concentrations at the grain boundary. This year we have addressed the issues with the previous version of the model, added a new term that accounts for the nucleation of dislocations at stress raisers (e.g., triple junctions) within the microstructure and discussed where there was disagreement in the literature about the underpinning physics (uranium self-diffusion at the grain boundary).

Attached below is a manuscript which we will submit for publication. The model outlined in the manuscript was also described using analytical fits and passed on to Idaho National Laboratory (INL) to be implemented in BISON. Furthermore, there is also surrogate modeling efforts being conducted by INL using this mechanistic creep model.

Diffusional creep in UO_2 informed by lower length scale simulations

Conor O.T. Galvin[a], David A. Andersson[a], Ryan Sweet[b], Laurent Capolungo[a], Michael W.D. Cooper[a]

[a]*Materials Science and Technology Division, Los Alamos National Laboratory, Los Alamos, NM 87545, USA*
[b]*Idaho National Laboratory, 1955 N Fremont Ave, Idaho Falls, ID 83415, USA*

Abstract

We present a diffusional creep model for UO_2 that has been informed using lower length scale simulations. The simulations focus on the uranium vacancy concentration, diffusivity and elastic dipole tensor, all of which underpin steady-state diffusional creep in UO_2. The results were compared against avaiable experimental values and used to provide insight where there is still some confusion, for example the uranium self-diffusion due to vacancies at grain boundaries. The ultimate objective of the work is not only to predict creep rates for different temperatures, grain sizes and stress, but also determine the dominant diffusional creep mechanism for UO_2, where there is disagreement in the literature. Creep is an important property for nuclear fuel performance as it influences the pellet-cladding gap, which in turn affects the fuel temperature. Having a creep model capturing the correct mechanisms is essential to be used in nuclear fuel performance codes. It is also an important first step towards modeling the complicated irradiation case, and is needed to support extension of the model to microstructures that have limited data.

1. Introduction

Uranium dioxide (UO_2) is the most common fuel type used in commercial light water reactors (LWRs) due to its suitable material properties, such as a high melting point, radiation tolerance, chemical stability and accommodation of non-stoichiometry and fission products [1]. Additionally there is the benefit of years of operational experience. Advanced fuels are currently being developed for use in LWRs to potentially provide better fuel performance and economics of operation. One of these advanced fuel candidates is doped UO_2, which has been doped to produce a larger grain size than conventional UO_2. The larger grain sizes provide improved operational fuel behavior for fission gas retention and pellet-cladding interactions due to improved mechanical properties [2]; one such property is creep. That is, having a 'softer' fuel pellet (higher creep rates) can reduce the risk of cladding failure by reducing the cladding-pellet mechanical interactions when the reactor undergoes a power ramp. Adding dopants can also increase the fuel density leading to less densification under irradiation [3]. Furthermore, extension of fuel burnups requires knowledge of how restructured fuel impacts properties including creep. For example, a characteristic of high burnup fuel is smaller grain sizes not just

Email address: (conor@lanl.gov)

in the periphery but also further towards the center of the pellet.

Creep is a type of plastic deformation of a solid material under stress. There are different mechanisms of creep and their significance depends on the material type and microstructure, for example metals or ceramics. In this study, we focus on the steady-state diffusional creep regime in UO_2. Diffusional creep has two different contributions: i) bulk diffusion (Nabarro-Herring [4, 5]) and ii) grain boundary diffusion (Coble [6]), illustrated in figure 1. In fact, Coble not only proposed the grain boundary diffusional creep mechanism generally, but also studies diffusional creep in UO_2 [7]. Both of these processes are driven by the net diffusion of uranium vacancies (although uranium interstitials may play an important role under irradiation conditions [8]) arising from the chemical potential gradient induced by an applied stress. However, there is still disagreement in the literature [7, 9–21] as to what is the rate-controlling mechanism in the diffusional creep regime of UO_2 (or if it even was a deformation mechanism). Not only is this important to understand if an accurate mechanistic creep model used to predict creep rates is to be developed, but Nabarro-Herring and Coble creep have different grain size dependencies. This would impact creep rates of doped UO_2, and undoped UO_2 which experiences grain growth if held at high temperatures [22] and grain sub-division at high burnup [23, 24]. In the case of doped UO_2 both the suppression of creep (due to large grains), the potential enhancement due to doping effects on defect chemistry (in the bulk or at the grain boundary) and grain sub-division at high burnup needs to be captured. A good handle on the correct mechanism (i.e. bulk or grain boundary) is needed to make better models.

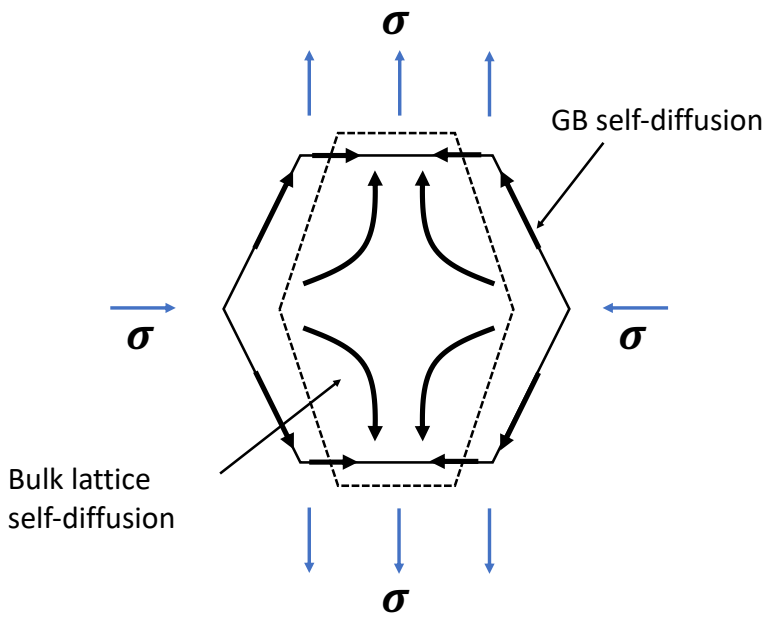

Figure 1: Schematic illustrating diffusional creep mechanisms occurring in a grain of UO_2.

Diffusional creep is also an interesting regime to study due to the underlying mechanisms which cause it. In UO_2 under thermal equilibrium conditions it is the concentration and diffusion of uranium defects (under an applied stress) which drive diffusional creep. For bulk UO_2 it is the uranium vacancies are the rate controlling diffusion process as they diffuse much

slower than oxygen atoms and are have concentrations than uranium interstitials [8]. However, for grain boundaries, to the best of our knowledge, this has not yet been shown, therefore, uranium vacancies and interstitials will be considered. Studying thermal equilibrium conditions is an important first step towards treating the more complicated irradiation case, which is relevant for fuel.

Not only does the expected uranium vacancy concentration and diffusion contribute to diffusional creep, but this diffusion process also impacts other important phenomena in UO_2, such as swelling due to fission gas release, bubble growth and sintering [25]. We predict this information, compare the uranium self-diffusion, D_U, to experiment, and discuss the reasons for the vast differences observed in the literature. For a clear comparison, in this study we will refer to the concentration of defects in the bulk as $[x]$, at the grain boundary as $[x_{GB}]$, the diffusion of a defect in the bulk as D_x, and at the grain boundary as D_x^{GB}. Therefore, the self-diffusion in the bulk is described as D_U^{bulk}, and the self-diffusion at the grain boundary is D_U^{GB}. The overall (volume) self diffusivity, D_U^v is then dependent on , D_U^{bulk}, D_U^{GB}, the grain boundary thickness (δ) and the grain size (G), as illustrated in figure 2.

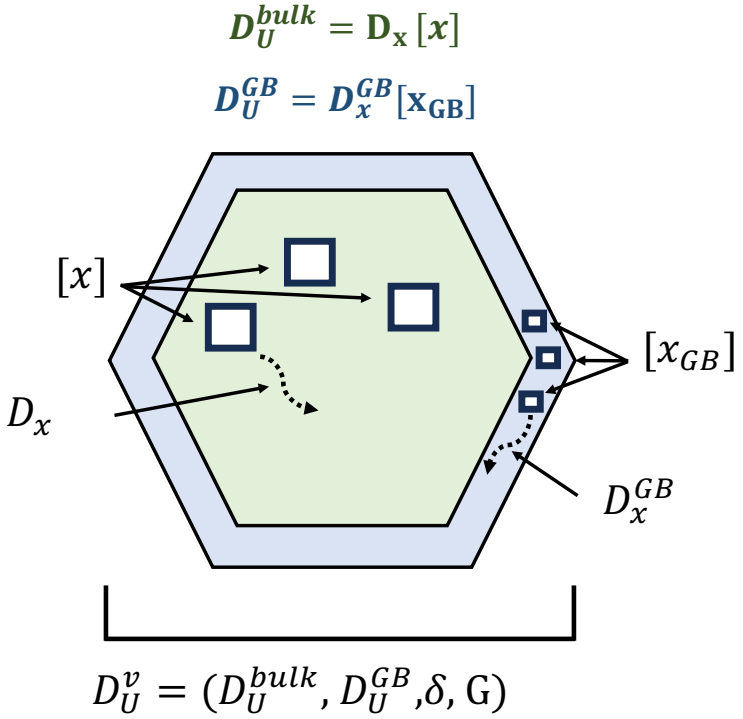

Figure 2: Schematic illustration of the processes that make up uranium self-diffusion in the grain, at the grain boundary and across the total volume of the grain for UO_2.

In this work, we use atomic-scale data to predict and understand the contributions that underpin the diffusional creep regime in UO_2. The main contributions being, the uranium vacancy defect concentration and diffusion, both in the bulk and at the grain boundary. The predictions are also compared with experimental results and discussed where there is still confusion, for example, the diffusion of uranium vacancies at UO_2 grain boundaries. The driving force for

diffusional creep studied here is the strain dependence of the chemical potential for uranium vacancies, given by the elastic dipole tensor of the uranium vacancy. This is widely known for uranium vacancies in the bulk [26], but it has not been studied for grain boundary uranium vacancies before. All the lower-length scale information is then used to develop a diffusional creep model for UO_2, where the model elucidates the dominant creep mechanism and is able to reproduce experimental data, thus, resolving the debate in the literature regarding the cause of diffusion creep in UO_2. This mechanistic model was validated against experimental results and can be used to predict creep rates in the diffusional regime of UO_2 as a function of temperature, stress and grain size.

2. Method

In this section the analytical creep equations and the lower-length scale computer simulation methods used to obtain the relevant data employed in the mechanistic diffusional creep model are discussed. Primarily, the diffusion coefficients, concentrations and elastic dipole tensor of uranium vacancies in the bulk and at the grain boundary. $\Sigma 9$ (221)/[110] and $\Sigma 11$ (311)/[110] symmetric tilt grain boundaries were deemed suitable choices for this study as they are common in UO_2 [27, 28] and do not induce a dipole like $\Sigma 5$ tilt grain boundary [29].

2.1. Analtical creep equations

For the diffusional creep model considered in this study the polycrystal behavior has been simplified into analytical equations. Ideally, a polycrystal plasticity model informed by lower length scale simulations should be used to capture the complex creep mechanisms. However, first we need to establish a baseline that ascribes creep in UO_2 to the correct mechanisms and shows that the lower length simulations are capable of capturing the relevant phenomena. Therefore, rather than tracking the response of local vacancy concentrations at grain boundaries and in the bulk due to applied stress, we instead predict average uranium vacancy defect concentration and diffusion coefficient in the bulk and at the grain boundary. Uranium interstitials are also included in our study. This information is then applied in the analytical creep equations (equations 1 and 2) outlined below, where stress, grain size and temperature is accounted.

Nabarro-Herring (bulk diffusional) creep occurs via the bulk diffusion of point defects within a grain in response to an applied stress. Defect concentration gradients arise across the grain due to the influence of stress on a defect's chemical potential. For example, the energy of vacancies is typically lower in a compressive strain field and, therefore, will diffuse from tensile to compressive regions. Consequently, uranium atoms will diffuse in the opposite direction, resulting in the transport of mass to tensile regions. This process results in plastic deformation (creep) that acts to relive an applied stress. The Nabarro-Herring creep rate, due to a given defect x can be approximated by the following equation [4, 5, 30]:

$$\dot{\epsilon}_{NH,\,x} = \frac{42|\Omega_x|D_x[x]}{k_B T G^2}\sigma_v \tag{1}$$

where σ_v is the von-Mises stress, G is the grain size, $[x]$ is the defect concentration, Ω_x is the defect volume, D_x is the diffusivity of defect x, k_B is the Boltzmann constant and T is temperature.

Coble creep is similar to Nabarro-Herring creep, however, rather than occurring within the grain interior, it transpires at the grain boundary. As with the Nabarro-Herring process, vacancies will diffuse (this time along the grain boundary), from tensile to compressive regions leading to transport of mass and creep. The Coble creep rate due to a given defect, x, is given by [6, 30]:

$$\dot{\epsilon}_{Coble,\,x} = \frac{42|\Omega_{GB,x}|D_x^{GB}[x_{GB}]\pi\delta}{k_B T G^3}\sigma_v \tag{2}$$

where $[x_{GB}]$ is the defect concentration at the grain boundary, Ω_x is the defect volume, D_x^{GB} is the is the diffusivity of defect, x, at the grain boundary and δ is the grain boundary thickness.

2.2. Simulation details

A cluster dynamics model formulated in terms of the free energy of the system (free energy cluster dynamics or FECD) developed by Matthews et al. [8] is implemented in the Centipede code. Centipede contains high fidelity atomistic simulations of point defect energies/entropies and information relating to the diffusion coefficient, such as, attempt frequencies and activation enthalpies, where the statistics is assumed to obey a point defect model. Centipede's main utility is under irradiation, however, here it is used for the thermal equilibrium state to calculate a charge neutral combination of defect concentrations in the bulk at a given temperature and oxygen partial pressure. In addition, it is also used to predict the diffusion coefficient for uranium defects. A more detailed description of Centipede can be found in [8].

Molecular dynamics (MD) simulations and static energy minimization calculations were carried out using LAMMPS [31] to calculate the uranium vacancy diffusion coefficients at a grain boundary, $D_{V_U}^{GB}$,the segregation energy of defects to the grain boundary (used to predict the defect concentrations, $[x_{GB}]$) and the elastic dipole tensor. For MD simulations the interatomic forces between all the U^{4+}-U^{4+}, O^{2-}-O^{2-} ions and the cross terms were described using the Cooper, Rushton and Grimes (CRG) potential [32]. U^{4+} ions are converted to U^{5+} for simulations which consider electron holes, denoted by $U_U^{\bullet}$ in Kröger-Vink notation [33]. The U^{5+} - O^{2-} and U^{5+} - U^{5+} interactions used are given by Liu et al. [34, 35]. As there is no U^{3+} (U_U' in Kröger-Vink notation) empirical potential compatible with the CRG, electron interactions described by changing the charge state of U^{4+} to U^{3+} are employed using the Gd^{3+}- O^{2-} parameters developed by Rushton and Chroneos [36]. This is assumed to be an appropriate assumption given the similar ionic radius of Gd^{3+} and U^{3+} [37]. A cut-off of 11 Å was employed for Coulombic interactions, which were calculated using a particle-particle particle-mesh solver at an accuracy of $1{\times}10^{-5}$.

2.2.1. Uranium Vacancy diffusion calculations

The diffusivity of a uranium vacancy D_{V_U} in the bulk is calculated from the DFT migration barriers [8, 38], the attempt frequency, the species dependent parameter jump distance and the number of jump sites while MD simulations are used to calculate the diffusivity of a uranium vacancy $D_{V_U}^{GB}$, at the grain boundary. The timescales are too slow to predict bulk uranium vacancy diffusivity using MD.

For the grain boundary MD simulations, symmetrical tilt grain boundary structures were generated with a rotation angle θ equal to half the misorientation angle. Two tilt grain boundaries common in UO_2 [27, 28], were considered for this study, and are outlined in table 1. Due

to the periodic boundary conditions, each simulation box contains two grain boundaries in the (y, z) plane, separated by a distance equal to half the box size along the x-direction. First, the lowest energy structure for each grain boundary type without any defects was found by sampling the γ-surface. This is achieved by shifting all atoms for one grain in the y-z plane with 0.5 Å increments and energy minimizing the system. Using the lowest energy minimized grain boundary structures from the γ-surface sampling, uranium vacancies were randomly added to the grain boundary (assuming a 1 nm thickness) at a specific concentration. As there are two grain boundaries in the structure (due to the periodic boundaries) vacancies were added to both. To observe the effects of different charge compensation mechanisms, structures containing $V_O^{\bullet\bullet}$ by removing oxygen atoms, $U_U^{\bullet}$ by converting some U^{4+} cations to U^{5+} describing the oxidation of U^{4+}, and applying a background charge were all created. These results are shown and discussed in the supplementary information.

Table 1: Supercell dimensions for the grain boundary structures. Each value in the dimensions refer to the x, y and z direction respectively (i.e. $L_x \times L_y \times L_z$) with the units in Å.

GB	Dimensions (Å)
Σ9-(221)	140.0×131.0×38.5
Σ11-(311)	178.9×181.5×46.3

Uranium vacancy diffusivities presented in the results section were calculated using MD simulations on the lowest energy position on the gamma surface for a given grain boundary containing uranium vacancies. Firstly, an MD run with an isobaric-isothermal (NPT) ensemble was carried out for 80 ps. The first 40 ps were used to bring the system from 300 K up to the desired temperature and then the system was allowed to equilibrate at the target temperature for 40 ps. An average of the lattice parameter was taken over the last 6 ps, and the structure lattice parameter was changed to the obtained average. The simulation was then run using a canonical (NVT) ensemble for 20 ps at the desired temperature and a microcanonical ensemble (NVE) for 70 ns (this time was reduced for some high temperature runs as we have enough statistics to get a linear mean squared displacement). From this, the mean squared displacement (MSD) for uranium was calculated and the uranium vacancy diffusivity was determined using equation 3.

$$D_{V_U}^{GB} = \frac{N_{tot}}{N_{GB}} \left(\frac{\langle R_{U_{yz}} \rangle}{4t} \right) \left(\frac{1}{[x_{GB}]} \right) \tag{3}$$

where N_{tot} is the total number of atoms in the system, N_{GB} is the number of atoms in the grain boundary, N_{tot}/N_{GB} = grain boundary thickness (δ) divided by the length of the supercell (x), $\langle R_{U_{yz}} \rangle$ is the MSD for uranium atoms in the yz plane, t is time and $[x_{GB}]$ is concentration of uranium vacancies, x, at the grain boundary (percentage of uranium vacancies with respect to uranium sites in the grain boundary). Generally, the mean-square displacement becomes a linear function of time as time increases so that the diffusion constant is simply related to the slope of this linear regime. It is important to run the simulation long enough that the linear regime is reached.

2.2.2. Uranium vacancy concentration calculations

The concentrations of uranium vacancies in the bulk are calculated using their formation energies, solving for charge neutrality and applying to an Arrhenius Law.

We assumed that the grain boundary and the bulk lattice are in thermal equilibrium, whereby the reduction in energy of a vacancy moving from the bulk to the grain boundary (segregation energy) couples the bulk and grain boundary concentrations. Therefore, the concentration of uranium vacancies at the grain boundary can be described by the formation energy of that defect in the bulk and its segregation to the grain boundary. The grain boundary uranium vacancy concentration at a given grain boundary site was calculated with the equation:

$$[x_{GB,site}] = exp\left(\frac{-(E_{f_{Bulk}} + E_{Seg,site})}{k_B T}\right) \tag{4}$$

where the segregation energy of defects to the grain boundary is

$$E_{Seg} = E_{f_{GB}} - E_{f_{Bulk}} \tag{5}$$

$E_{f_{Bulk}}$ refers to the formation energy of the defect in the bulk and $E_{f_{GB}}$ is the formation energy of the defect at the grain boundary.

Alternatively, if the bulk concentration is know (which is predicted), the grain boundary concentration can be expressed at each grain boundary site as:

$$[x_{GB,site}] = exp\left(\frac{-E_{Seg,site}}{k_B T}\right)[x] \tag{6}$$

where $[x_{GB,site}]$ is the concentration of defects at a grain boundary site and $[x]$ is the concentration of uranium vacancies in the bulk. Any site that had a concentration greater than 1 was set to the value of 1. Then the average concentration of uranium vacancies across the whole grain boundary is given by the mean concentration across all grain boundary sites:

$$[x_{GB}] = \sum_{sites} \frac{[x_{GB,site}]}{n_{sites}} \tag{7}$$

where n_{sites} refers to the total number of grain boundary sites.

However, just having the uranium vacancies segregate to the grain boundary would result in an unphysical build up of charge. Therefore, a charge neutral combination of oxygen, uranium, electron, and hole defects, at the grain boundary must be solved for. This includes their segregation energies to the grain boundary. The energy for each defect (presented in table 2) at a given site in the grain boundary was calculated by either i) removing an atom for a vacancy, ii) adding an atom for an interstitial or, iii) changing the charge state of the uranium to 3^+ or 5^+ for an electron or a hole, and carrying out static geometry optimization. This process was repeated for all the available sites in both the $\Sigma 9$ and $\Sigma 11$ supercells, as outlined in table 3.

Table 2: Defects used for segregation energy calculations.

Defect type	Formal charge	Kröger-Vink notation
Uranium vacancy	4^-	V_U''''
Uranium interstitial	4^+	$U_i^{\bullet\bullet\bullet\bullet}$
Oxygen vacancy	2^+	$V_O^{\bullet\bullet}$
Oxygen interstitial	2^-	O_i''
Electron	1^-	U_U'
Hole	1^+	$U_U^{\bullet}$

Table 3: Supercell dimensions for grain boundary structures used for segregation energy calculations.

Grain boundary	Dimensions (Å)
Σ9-(221)	186.3×32.7×23.1
Σ11-(311)	180.9×25.6×23.1

To enforce charge neutrality at the grain boundary, an electron potential solver which adjusts the Fermi level depending on the total defect concentration is applied. The charge of a defect, q_x, multiplied by the electron potential, μ_e, is applied to the segregation energy by the following equation:

$$[x_{GB,site}] = exp\left(\frac{(-E_{Seg,site}) + (q\mu_e)}{k_B T}\right)[x] \tag{8}$$

The total charge concentration at the grain boundary, Q_{GB} is given by:

$$Q_{GB} = \Sigma q_x [x_{GB}] \tag{9}$$

The electron potential, μ_e, is iteratively refined until $Q = 0$ ensuring that the concentrations of all defects in the grain boundary are fully charge compensated.

To make sure there is not a discontinuity between the grain boundary and the bulk after shifting μ_e to get a charge neutral combination of defects at the grain boundary, μ_e is weighted changing fractionally from the bulk to the grain boundary, as illustrated in figure 3. That is, closer to the bulk μ_e is slightly shifted, with the greatest contribution to μ_e occurring at the grain boundary center. The Fermi level at the bulk comes from $[x]$, shown in equation 2.2.2.

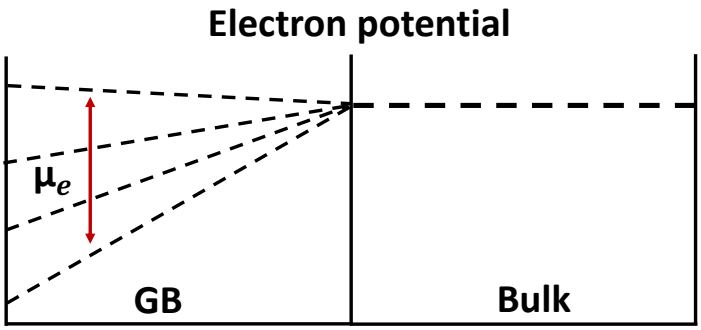

Figure 3: Schematic illustrating the fractional change in μ_e from bulk to the grain boundary.

2.3. Elastic dipole tensor

As mentioned earlier, the elastic dipole tensor describes the change in defect energy due to an applied strain. This can also occur at the grain boundary and, therefore, provides a thermodynamic driving force for Coble creep whereby defects migrate in response to, and relive, an applied stress. The grain boundary structure used for the elastic dipole tensor calculations is given in table 4.

Table 4: Supercell dimensions for grain boundary structures used for elastic dipole tensor calculations.

Grain boundary	Dimensions (Å)
Σ11-(311)	180.8×25.6×23.1

Similar to the segregation energy calculations, for the grain boundary structure, a uranium atom was removed from the system to create a point defect. This was carried out separately for all .uranium sites in the structure, such that up to 4000 separate structures were generated containing one vacancy each. The defective grain boundary structure was then energy minimized, while keeping the supercell dimensions fixed. Following this, the supercell was strained to determine the response of the vacancy formation energy to the three orthogonal and three shear strains. The tensor that describes the strain-response of the vacancy formation energy can be described as an effective elastic dipole tensor, $\mathbf{G}^*$. It is not strictly a true elastic dipole tensor, $\mathbf{G}$, as we are investigating the response due to the strain applied to the supercell, rather than resolving the strain at the location within the grain boundary where the defect is sited. Nonetheless, it is the response to strains at the supercell length scale given by $\mathbf{G}^*$ that is relevant for implementation in the diffusion-mediated creep model. A specific component of $\mathbf{G}^*$ for a uranium vacancy with its formal -4 charge is given by:

$$\mathbf{G}^*_{ij} = -\frac{\partial E_{V''''_U}}{\partial \epsilon_{ij}} \tag{10}$$

where,

$$E_{V''''_U} = E_{def} - E_{perf} \tag{11}$$

E_{def} and E_{perf} are the energies of the defective and perfect supercells at a given strain, respectively. Note that although the formation energy also contains terms for the reference energies, such as uranium metal or O_2; these terms are independent of the stress state of the material and are, thus, not included in the calculation of $\mathbf{G}^*$. In addition to examining $\mathbf{G}^*$ for V''''_U, it is also necessary to determine $\mathbf{G}^*$ for $U^{\bullet}_U$ ions. Exactly the same procedure as described above for V''''_U was employed for $U^{\bullet}_U$. It is critical to include $U^{\bullet}_U$ so that the flow of charge neutral combinations of defects can be accounted for; thus, preventing unphysical charge build up when simulating diffusional creep.

3. Results and Discussion

3.1. Diffusivity of a uranium vacancy

The prediction of uranium vacancy diffusivity, D_{V_U}, in the bulk is shown by the green line in figure 4. Bulk defect diffusivity, D_{V_U} values were calculated for each contributing defect type using the DFT migration barriers and empirical potential calculated entropies [8].

The grain boundary uranium vacancy diffusion coefficient, $D^{GB}_{V_U}$, was calculated at two symmetric tilt grain boundaries, Σ9 and Σ11 (see table 1). Three different charge compensating mechanisms were tested and it was found that the type of charge mechanism (structures containing $V^{\bullet\bullet}_O$, $U^{\bullet}_U$ and applying a background charge) does not greatly affect $D^{GB}_{V_U}$ (these results are presented in the supplementary information). Therefore, the charge compensation mechanism chosen to be applied going forward was a net background charge. Furthermore, different

concentrations and temperatures were examined to see if they impact the predicted $D_{V_U}^{GB}$, making sure to capture $D_{V_U}^{GB}$ values in the point defect limit. A concentration of 0.25% uranium vacancies was decided to be used to ensure that the vacancies did not interact. These results are also shown in the supplementary information. Using MD, there needs to be enough vacancies in the system, so that sufficient statistics can be obtained at a given temperature to calculate a $D_{V_U}^{GB}$ value during timescales associated with MD (on the order of 10s of ns).

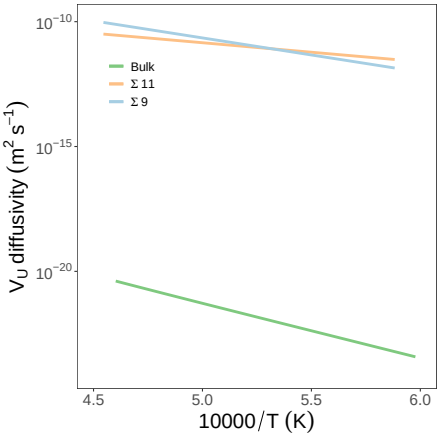

Figure 4: Arrhenius plot of uranium vacancy diffusion coefficient as a function of inverse temperature.

Figure 5a shows the MSD for uranium atoms at the Σ9 tilt grain boundary structure across the temperature range 1600-1900 K. The uranium atoms do not move in the bulk because there are no vacancies there, and $D_{V_U}^{GB}$ is much lower in the bulk compared to the grain boundary, as shown in figure 4. It can be seen that for lower temperatures (<1800 K) a timescale of ∼70 ns was needed to achieve enough statistics to observe proper linear behavior for lower temperature runs, and therefore, capture long range diffusion at the GB. The MSD was then used in equation 3 to calculate $D_{V_U}^{GB}$, shown as a function of temperature in figure 5b. From this a migration energy and pre-exponential, D_0^{GB} was calculated, which are presented in table 5.

The same procedure as outlined above was conducted for the Σ11 tilt grain boundary. The MSD of the uranium atoms are shown in figure 6a, with the corresponding uranium vacancy diffusion coefficient presented in figure 6b. Under thermal equilibrium conditions, it is the uranium vacancies (and not interstitials) that will dominate due to their concentration, as will be discussed in the next section. However, uranium interstitials may play an important role under irradiation conditions and this will be examined in a future study.

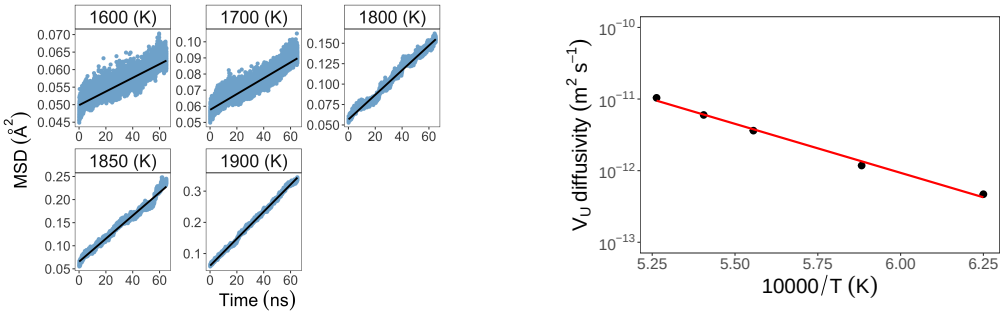

(a) (b)

Figure 5: (a) Mean squared displacement of uranium atoms in a Σ9 tilt GB containing uranium vacancies at different temperatures. (b) Uranium vacancy diffusion coefficient as a function of inverse temperature in a Σ9 tilt grain boundary.

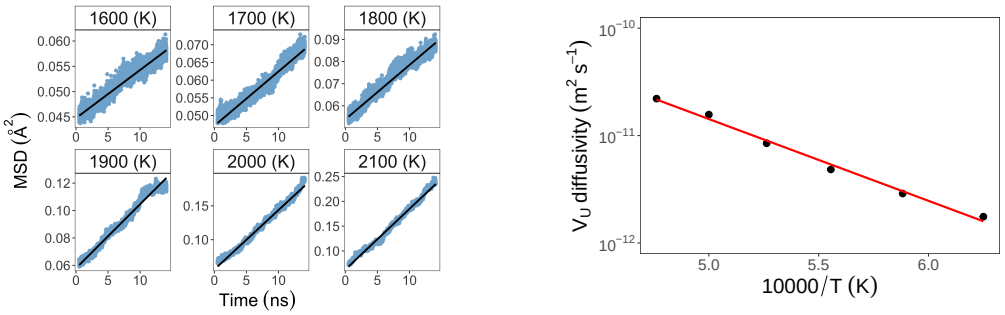

(a) (b)

Figure 6: (a) Mean squared displacement of uranium atoms in a Σ11 tilt GB containing uranium vacancies at different temperatures. (b) Uranium vacancy diffusion coefficient as a function of inverse temperature in a Σ11 tilt grain boundary.

Table 5: $D_{V_U}^{GB}$ pre-exponential and migration energy values calculated from figures 5b and 6b. The grain boundary thickness was calculated from the segregation energy calculations shown in the supplementary information.

GB	D_0^{GB} m^2/s	E_{mig} eV	GB thickness nm
Σ9	1.50×10^{-4}	2.71	3
Σ11	9.13×10^{-8}	1.51	4

Plotting the diffusion coefficient of a uranium vacancy, on a log scale as a function of 1/T, as presented in figure 4 lets us compare the diffusion at the grain boundary to that in the bulk. Figure 4 shows that, for both grain boundary cases, $D_{V_U}^{GB}$ is orders of magnitude greater than that in the bulk. Furthermore, it is observed that different grain boundaries will have different $D_{V_U}^{GB}$ values, however, they are still orders of magnitude greater than the bulk. This result indicates that Coble creep rates will be shifted to higher values compared to the Nabarro-Herring creep rates - a point that will be discussed in greater detail later in this study.

3.2. *Uranium vacancy concentrations*

The bulk uranium vacancy concentration that the Centipede code predicts is shown as a function of inverse temperature by the green line in figure 7a. The partial pressure as a function of temperature was taken as the "best case" from Matthews et al. [8], at a value of H_{PO2} =5.9 eV and T_0=2373 K. The "best case" conditions produced uranium self-diffusivity data that matches the uranium self-diffusion (D_U^{bulk}) experimental data from Sabioni et. al [39].

To predict the defect concentrations at the grain boundary, first the segregation energies for each defect listed in table 2 at the Σ9 tilt and Σ11 tilt grain boundaries (shown in table 3) are needed. The segregation energy as a function of site filling (energy from lowest to highest) for the different point defects are presented in the supplementary information. Figure 7a shows the grain boundary uranium vacancy concentrations, $[V_{U,GB}]$ plotted alongside the uranium vacancy concentrations in the bulk, $[V_U]$. It can be seen that the grain boundary concentrations are orders of magnitude greater than those in the bulk. Again, like the enhanced grain boundary diffusivity, this suggests that Coble creep might be the dominant diffusional creep mechanism. The two grain boundary structures have a large difference in the concentrations, where Σ 11 shows stronger segregation of uranium vacancies.

Figure 7b shows the grain boundary uranium interstitial concentrations, $[U_{i,GB}]$ plotted alongside the uranium interstitial concentrations in the bulk, $[U_i]$. A similar trend is seen as for the uranium vacancies shown in figure 7a, in that there is an enhancement for the concentration at the grain boundary compared to the bulk. However, these interstitial concentrations are orders of magnitude lower than the vacancies, therefore will likely not contribute to the diffusional creep rates.

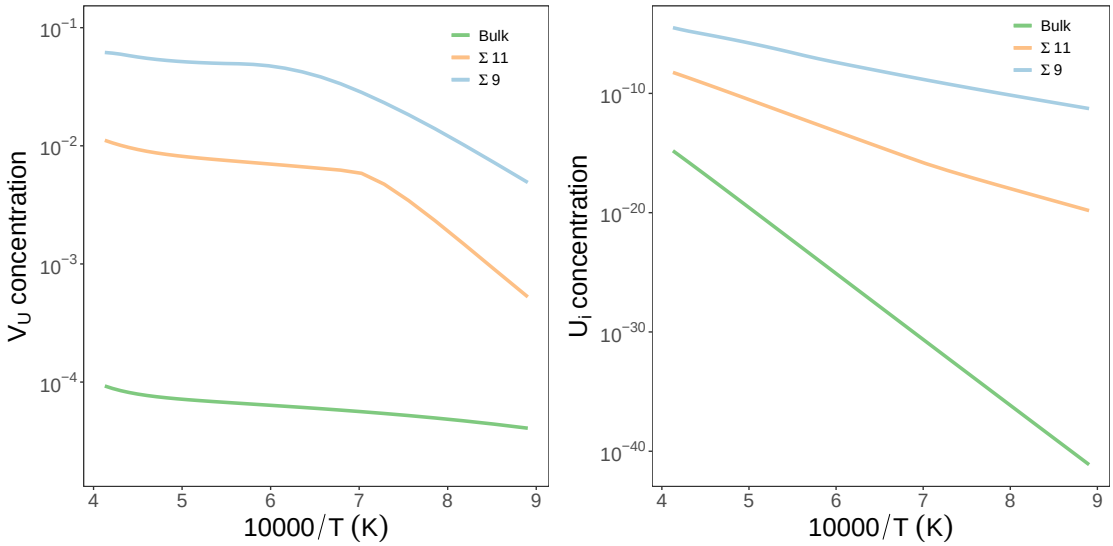

Figure 7: (a) An Arrhenius plot of the uranium vacancy concentration as a function of inverse temperature.(b) An Arrhenius plot of the uranium interstitial concentration as a function of inverse temperature.

3.3. *Uranium self-diffusion*

Figure 8 shows a plot of our lower length-scale uranium vacancy grain boundary self-diffusion (shown by the dotted gray lines), $D^{GB}_{U,V_U} = D^{GB}_{V_U}[V_{UGB}]$, plotted against a number of studies showing uranium self-diffusion (volume, single crystal and grain boundary) in UO_2. In addition, uranium self-diffusion coefficients inferred from creep experiments are also presented. They were calculated by backing out a D_U value from equations 1 or 2 depending on the assumed dominant mechanism.

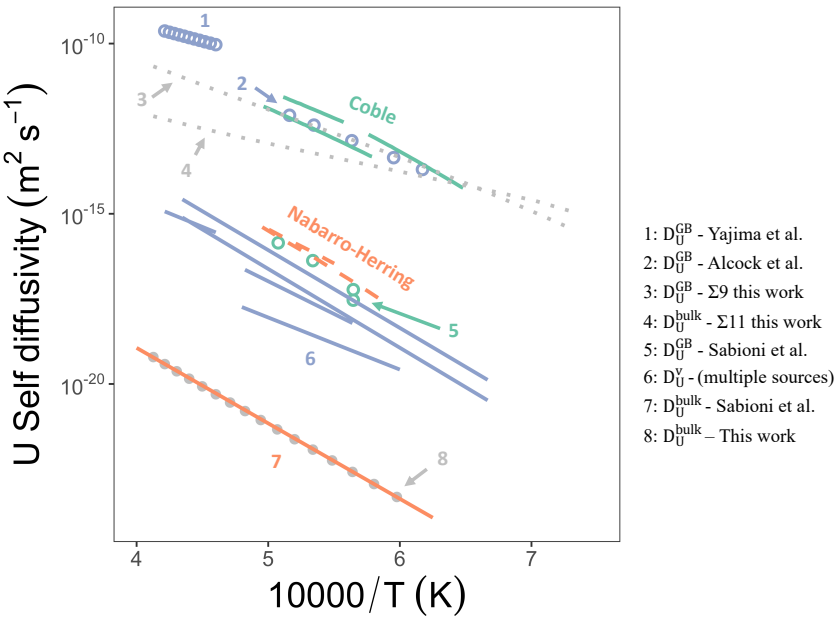

Figure 8: Uranium self-diffusion as a function of inverse temperature. The solid green and dashed orange lines represent the uranium self diffusivity backed out of different experimental creep rates [9, 12, 14, 40] using equations 1 and 2. The circles represent calculated grain boundary results from tracer experiments. The solid purple lines are volume diffusivity tracer experiment results [41–45] in polycrystalline material. The solid orange line is the bulk result from a tracer experiment in single crystal. The dotted grey lines are results using our grain boundary diffusion coefficients and concentrations.

It was observed in a tracer experiment of uranium grain boundary self-diffusion by Sabioni et al. [46] (green circles) is comparable to most total volume uranium self-diffusion, D^v_U, coefficients in polycrystalline UO_2 (purple lines, labeled 6). This suggests that grain boundaries have a greater impact on the uranium self diffusivity in polycrystalline materials then was previously assumed and is discussed extensively by Sabioni et al. [46]. Moreover, single crystal data (pure bulk) from Sabioni et al. [39] show a much lower diffusivity (orange solid line, labeled 7) compared to the polycrystalline materials.

Note that the uranium self-diffusion values inferred from experiments assuming a Coble (grain boundary) creep mechanism (green solid lines) are orders of magnitude higher than the tracer diffusivity experiment results measured for grain boundaries by Sabioni et al. [46] (green circles, labeled 5) and the polycrystalline UO_2 data (purple lines, labeled 6). Additionally, the uranium self-diffusion values inferred from experiments assuming a Nabarro-Herring (bulk)

creep mechanism (orange dashed lines) are also orders of magnitude greater than the single crystal data (bulk) from Sabioni et al. [39] (orange solid line labeled 7). When compared to our D^{GB}_{U,V_U} simulation results (gray dotted lines) there is good agreement with the experimental data when assuming a Coble mechanism (green lines). Moreover, grain boundary diffusion coefficients by Alcock et al. [45] and Yajima et al. [44] (purple circles, labeled 1 and 2) also compare well with the uranium self-diffusivity inferred from creep experiments, assuming a Coble mechanism, and with our modeling predictions. However, there is uncertainty whether the grain boundary data by Alcock et al. and Yajima et al. is applicable or not as it was calculated using high values for the volume diffusion coefficients (purple lines, labeled 6) and did not account properly for the effect of grain boundaries as is discussed in [46].

Despite this, there is a clear discrepancy between the grain boundary tracer self-diffusivity by Sabioni et al. and the polycrystalline UO_2 data, compared to the self-diffusivity inferred from creep experiments when a Coble mechanism is assumed. There are a number of explanations that might account for this. For example, when Sabioni et al. [46] measured uranium self-diffusion at a grain boundary, it is measured as the diffusivity multiplied by a grain boundary thickness. The grain boundary thickness assumed in the work by Sabioni et al. [46] was 1 nm, however, this would have to change by orders of magnitude to be comparable to the uranium self-diffusion values inferred by the Coble creep experiments shown in figure 8, so is unlikely to be the cause. Another possible explanation is that the impact of grain boundaries is not being correctly accounted for in the volume uranium self-diffusion coefficients. However, this also seems unlikely to cause a difference by orders of magnitude.

The main cause for the difference in the data seems to be the impact of stoichiometry. Figure 9 shows the uranium vacancy self-diffusivity, D^{GB}_{U,V_U}, plotted as a function of stoichiometry for two different temperatures using the Σ 11 grain boundary case. There is a huge stoichiometry dependence (orders of magnitude) on the self-diffusivity, especially around an O/M value of 2. In reality, it is extremely difficult to maintain perfect stoichiometry of UO_2 and experiments have a resolution of roughly $UO_2 \pm 0.001$ [47], and it is clear from figure 9 that in this range the self-diffusivity can vary by orders of magnitude. Therefore, the scatter in the data shown in figure 8 is likely to be caused by the slight non-stoichiometry of UO_2. The impact of stoichiometry on creep rates will be discussed in greater detail later in this study.

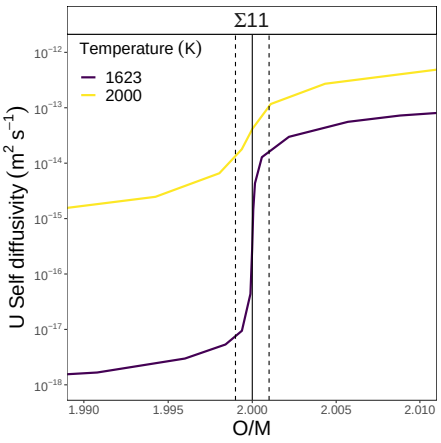

Figure 9: D_U^{GB} as a function of O/M for the Σ 11 case. The color represents the temperature. The dashed lines are the usual experimental 'nominally' stoichiometric resolution.

3.4. Elastic dipole tensors

To predict the elastic dipole tensor, first we studied the response of V_U'''' and $U_U^{\bullet}$ formation energies to the stress state in bulk lattice for a 10×10×10 supercell using MD. The off-diagonal components of $\mathbf{G}^*_{V_U''''}$ and $\mathbf{G}^*_{U_U^{\bullet}}$ are all zero and the diagonal components are equal (see equations 12, 13 and 14), as expected for point defects in a cubic system. Given that four $U_U^{\bullet}$ are required to charge compensate a single V_U'''', it can be seen that the combined $\mathbf{G}^*$ for a charge-neutral grouping of defects, $\mathbf{G}^*_{V_U''''} + 4\mathbf{G}^*_{U_U^{\bullet}}$, would have negative diagonal components of -13.65 eV. This shows that the charge-neutral collective migration of V_U''''+ $4U_U^{\bullet}$ is expected to be from tensile to compressive regions, as is necessary for diffusional creep to occur. Next we include vacancies located at the grain boundary shown in table 4.

$$\mathbf{G}^*_{V_U''''} = \begin{pmatrix} 29.23 & 0.00 & 0.00 \\ 0.00 & 29.23 & 0.00 \\ 0.00 & 0.00 & 29.23 \end{pmatrix} \tag{12}$$

$$\mathbf{G}^*_{U_U^{\bullet}} = \begin{pmatrix} -10.72 & 0.00 & 0.00 \\ 0.00 & -10.72 & 0.00 \\ 0.00 & 0.00 & -10.72 \end{pmatrix} \tag{13}$$

$$\mathbf{G}^*_{V_U''''} + 4\mathbf{G}^*_{U_U^{\bullet}} = \begin{pmatrix} -13.65 & 0.00 & 0.00 \\ 0.00 & -13.65 & 0.00 \\ 0.000 & 0.00 & -13.65 \end{pmatrix} \tag{14}$$

The elastic dipole tensor components for a uranium vacancy corresponding to orthogonal and shear strains of the simulation supercell containing two Σ 11 grain boundaries (and segregation energies) are reported in the supplementary information. Here, we have attempted to construct an effective grain boundary elastic dipole tensor, $\mathbf{G}^{*GB}_{ij}$, that can account for the cumulative impact of all possible defect sites. To do so, a partition function based on the segregation

energy, E_{seg}, has been used to weight the contribution to the effective dipole tensor from a given defect site, $\mathbf{G}^{x}_{ij}$, as follows:

$$\mathbf{G}^{*GB}_{ij} = \frac{\sum_{\mathrm{n_{sites}}} \mathbf{G}^{x}_{ij} \exp\left(\frac{-E_{seg}}{k_B T}\right)}{\sum_{n_{sites}} \exp\left(\frac{-E_{seg}}{k_B T}\right)} \tag{15}$$

It can be seen that for the grain boundary studied, there is a significant change in the effective elastic dipole tensor for the grain boundary compared to the bulk. Not only is the impact of the grain boundary quantitative but there is a change in the sign of the G_{33} component (see equation 18). This indicates that for this grain boundary under a gradient in strain perpendicular to the grain boundary, V''''_U will diffuse in the opposite direction to vacancies under the same strain in the bulk. This statement applies only to vacancies that are not charge neutral. To consider the charge neutral flow of defects, one must also account for the influence of strain on the formation energy of charge-compensating $U^{\bullet}_U$, as will be discussed in the following section.

$$\mathbf{G}^{*GB}_{V''''_U} = \begin{pmatrix} 21.48 & -0.03 & 0.09 \\ -0.03 & 30.11 & 7.06 \\ 0.09 & 7.06 & 28.78 \end{pmatrix} \tag{16}$$

$$\mathbf{G}^{*GB}_{U^{\bullet}_U} = \begin{pmatrix} -9.04 & -0.09 & 0.06 \\ -0.09 & -8.76 & -0.02 \\ 0.06 & -0.02 & -6.03 \end{pmatrix} \tag{17}$$

$$\mathbf{G}^{*GB}_{V''''_U} + 4\mathbf{G}^{*GB}_{U^{\bullet}_U} = \begin{pmatrix} -14.68 & -0.39 & 0.33 \\ -0.39 & -4.93 & 6.98 \\ 0.33 & 6.98 & 4.66 \end{pmatrix} \tag{18}$$

The elastic dipole tensor at the grain boundary was then converted into an atomic volume Ω to be used in the Coble creep equation (equation 2) via [48]:

$$\Omega = \frac{1}{3K}(G_{11} + G_{22} + G_{33}) \tag{19}$$

where K is the bulk modulus (taken as 208.9 GPa [49]) and G_{11}, G_{22}, G_{33} are the trace of the tensor in equation 18.

3.5. Analytical Creep Model

In this section, the lower length-scale atomistic data is incorporated into the analytical creep equations 1 and 2, and the creep rates of UO_2 for the two diffusional mechanisms (Nabarro-Herring and Coble) as a function of grain size, stress and stoichiometry for different temperatures is predicted. Again, it is important to distinguish among the two creep mechanisms, given that they have different grain-size dependencies.

3.5.1. Contribution of Different Mechanisms to the Creep Rate

Creep rate as a function of grain size is presented in figure 10, at a stress of 10 MPa for two different temperatures. The creep rates are displayed as the different contributing mechanisms; Nabarro-Herring and Coble. Experimental 'nominally' stoichiometric creep rates from the study by Knorr et al. [7] are included under the same temperature and stress conditions for comparison. It can be seen from the plot that Coble creep is the dominant mechanism and compares well against the experimental points for both grain boundaries considered. It can be seen that at 2023 K the Coble model for the Σ 9 grain boundary has a better agreement with the experimental data indicating that there is a stronger temperature dependence for one grain boundary type compared to the other.

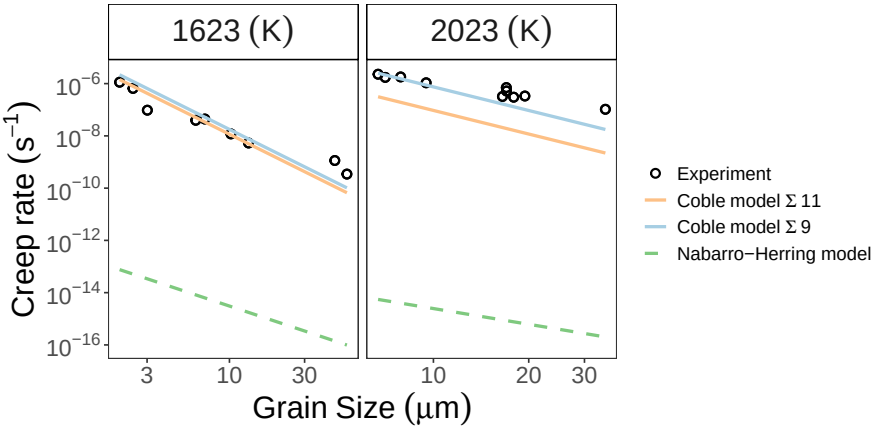

Figure 10: Creep rate as a function of grain size for two temperatures and at a stress of 10 MPa. The two creep mechanisms are represented by line type. Nominally stoichiometric experimental points from Knorr et al [7] are shown as black circles.

Shown in figure 11 is the creep rate predicted in the Coble regime (two grain boundaries) and Nabarro-Herring (bulk) as a function of bulk non-stoichiometry, for a stress of 10 MPa and grain size of 3 μm. It can be seen that for each mechanism there is an increase of creep rate as a function of increasing hyper-stoichiometry. This is because underpinning the creep rates for each mechanism are either grain boundary or bulk uranium vacancy concentrations, which are hyper-stoichiometric defects. In addition, both Coble and Nabarro-Herring are most sensitive to stoichiometry near to O/U=2. This indicates that although many experiments report near-stoichiometric creep data (O/U = 2 ± 0.01), it is still likely that significant variation can occur in this range, making direct comparison difficult. This sensitivity to O/U is more significant at lower temperatures. Furthermore, the sensitivity to O/U is more significant for the Σ 11 grain boundary compared to the Σ 9 grain boundary, showing that there is a grain boundary type dependency. In fact, for the Σ 11 grain boundary at a temperature of 1600 K the creep rates are higher than for the Σ 9 grain boundary in the hyper-stoichiometric region. This is why higher creep rates are seen for the Σ 11 Coble model compared to the Σ 9 Coble model in figure 12, where the opposite is seen in figures 10 and 13. Eventually, polycrystalline simulations should be carried out to examine the creep response of a microstructure containing a variety of different grain boundaries that exhibit different contributions to Coble creep and show different sensitivites to O/U. However, regardless of stoichiometry the Coble mechanism is dominant.

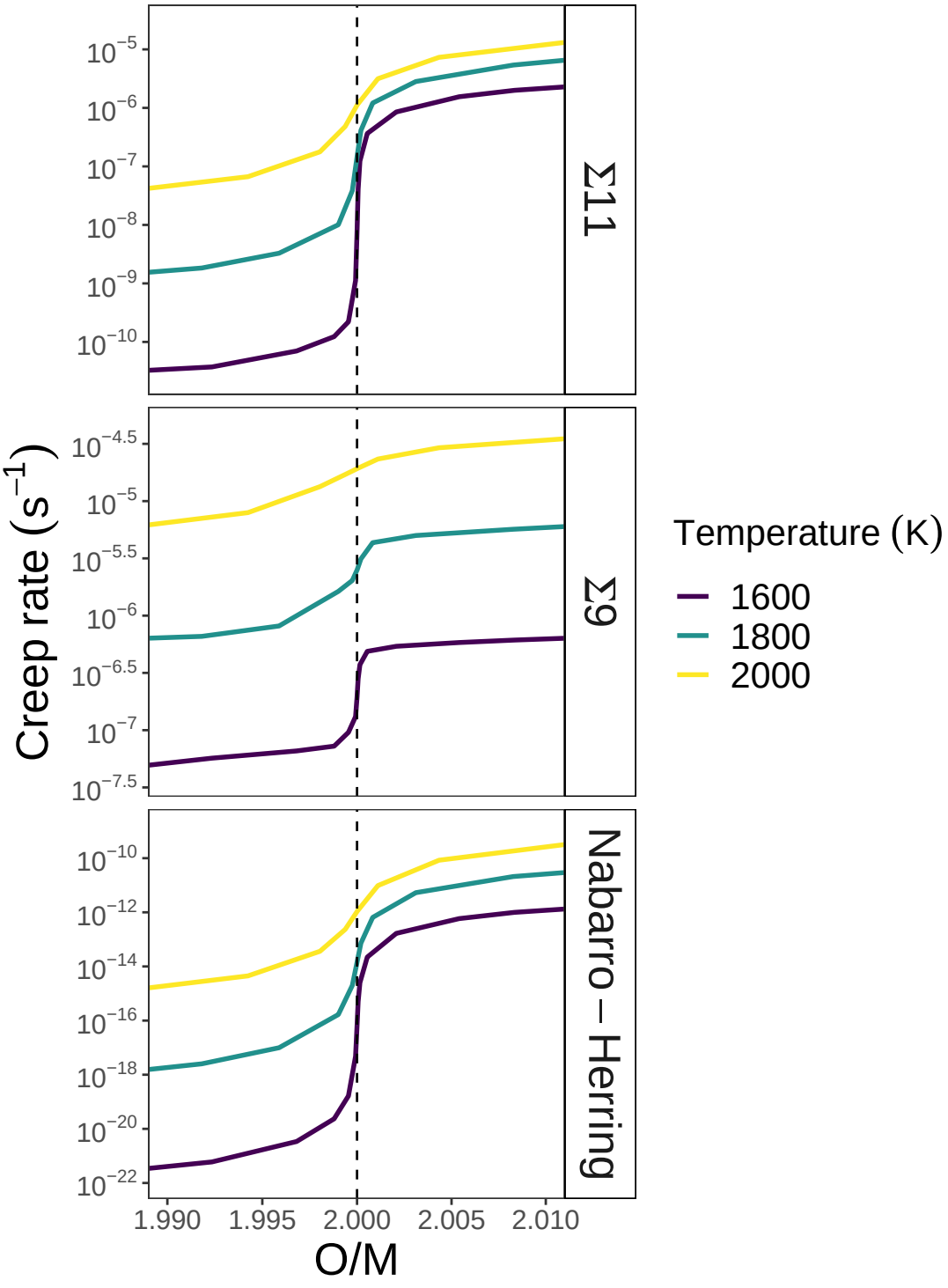

Figure 11: Creep rate as a function of bulk O/M. The color represents the temperature.

3.5.2. Validation of Creep Rate Model Compared to Experiment

The stoichiometry dependence of the Coble creep regime as a function of stress for two different temperatures is presented in figure 12. In figure 12 experimental creep rates [50] are shown as black circles while the solid points/lines represent the predictions from the mechanistic creep model. The trend of increasing creep rates as a function of increasing hyperstoichiometry is the same as experiment. Furthermore, the slight increase in creep rates with increasing stoichiometry, both from the model and experiment, also gives us confidence that the mechanistic model is predicting the correct behavior. There is a factor of ~5 difference in the experimental creep rates between $UO_{2.001}$ and $UO_{2.01}$ and there is also a small increase from the Coble contribution predicted by the model (although this increase is much smaller at 1573 K). A much larger contribution is seen for the Nabarro-Herring component shown in figure 11 (orders of magnitude), therefore, if Nabarro-Herring was to be the dominant mechanism we would expect to see a much larger deviation in stoichiometry from the experimental points. It is important to note we can only predict small deviations in stoichiometry, and if we push beyond these bounds the point defect energies that Centepide uses would not be valid (i.e. outside the point defect limit).

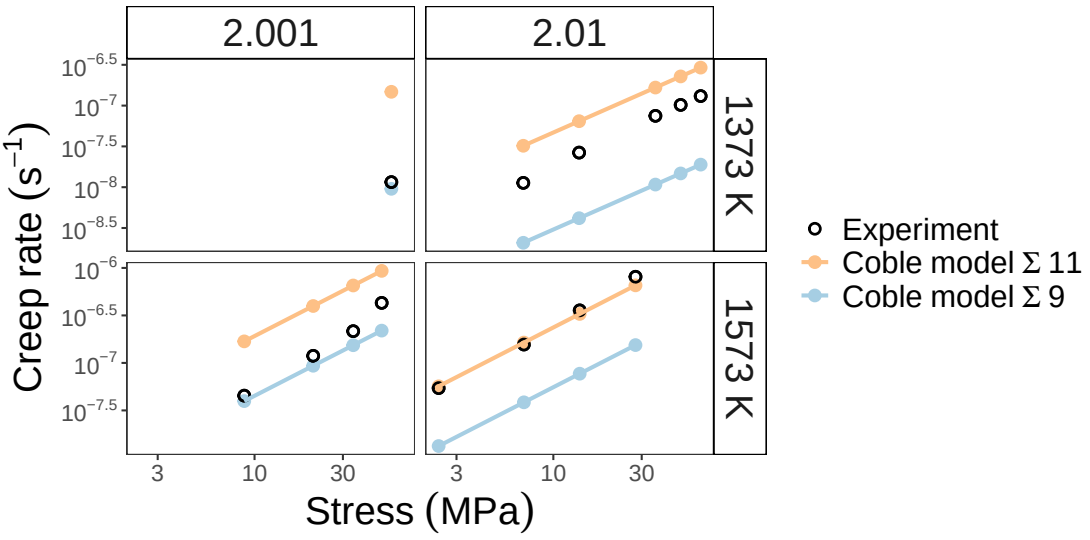

Figure 12: Creep rate as a function of stress for two different temperatures (1373 K and 1573 K) and stoichiometries (2.001 and 2.01) for a grain size of 7 μm. The solid points are the predictions from the mechanistic model while the open circles represent experimental data [50].

The total creep rate (summation of all contributions) predicted from our mechanistic model is compared to experimental data points as a function of grain size, temperature and stress in figure 13. Chung and Davies [14] report low-stress diffusional creep response for nominally stoichiometric UO_2 at temperatures ranging from 1273 - 1873 K for different grain sizes. Using these data, figure 13 compares creep rates from the atomistic informed creep mechanistic model to the experimental data over this range of stresses and grain sizes. Again, the partial pressure as a function of temperature was taken as the "best case" from Matthews et al. [8], at a value of H_{PO2} =5.9 eV and T_0=2373 K. For both grain boundaries the Coble models compare reasonably well to experiment with the Σ 9 grain boundary producing higher creep rates compared to the

Σ 11. This is consistent with figure 10 which uses the same oxygen partial pressure conditions.

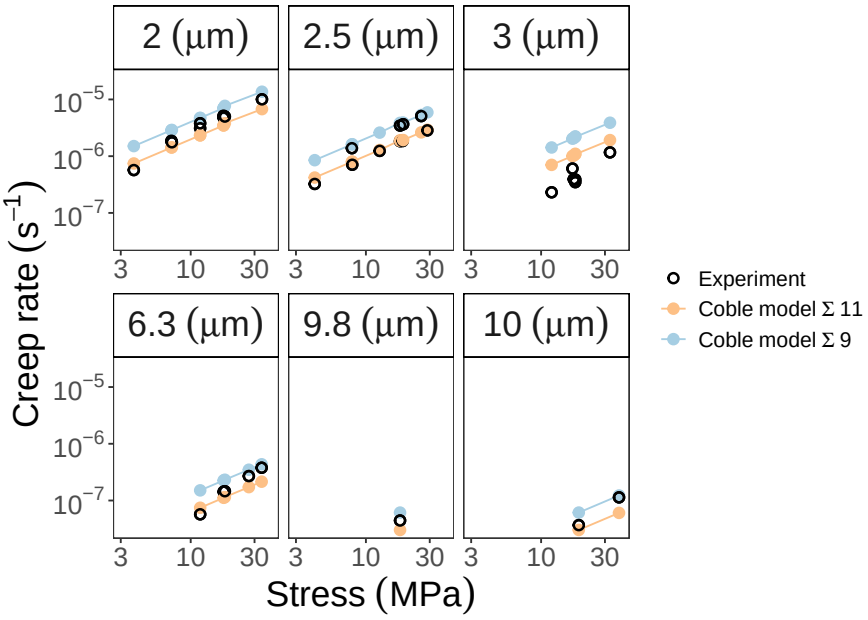

Figure 13: Predicted creep rate predicted from the mechanistic model (blue and orange solid points) as a function of grain size and stress at 1623 K compared with the data from Chung and Davies [14] shown by the black circles.

Figure 14 shows the creep rate from numerous experiments [9–14, 51, 52][1] against the creep rates predicted by the mechanistic model on a log-log plot in the diffusional regime with an O/M close to 2. In figures 14a and 14b the color represents the temperature and the shape represents the grain size. In figures 15a and 15b the color represents the stress that the creep rates were calculated at. It can be seen that the mechanistic model does a good job at describing creep over a range of experimental conditions considering: i) the model uses atomic scale parameters with no fitting, ii) simple analytical equations were used that include assumptions regarding uniform spherical grains, iii) it is not possible to exactly match the oxygen partial pressure that the experiments were carried out under. The model predictions deviate from experiment for temperatures below ~1700 K and at a grain size of around ~ 7µm. Similarly the model deviates from experiment at high temperatures and large grain sizes, >17µm. Figure 15 shows that the difference between the creep rates predicted by the model and experiment is not greatly affected by stress (in the diffusional regime).

[1] The experimental data has been filtered to only consider values in the diffusional regime

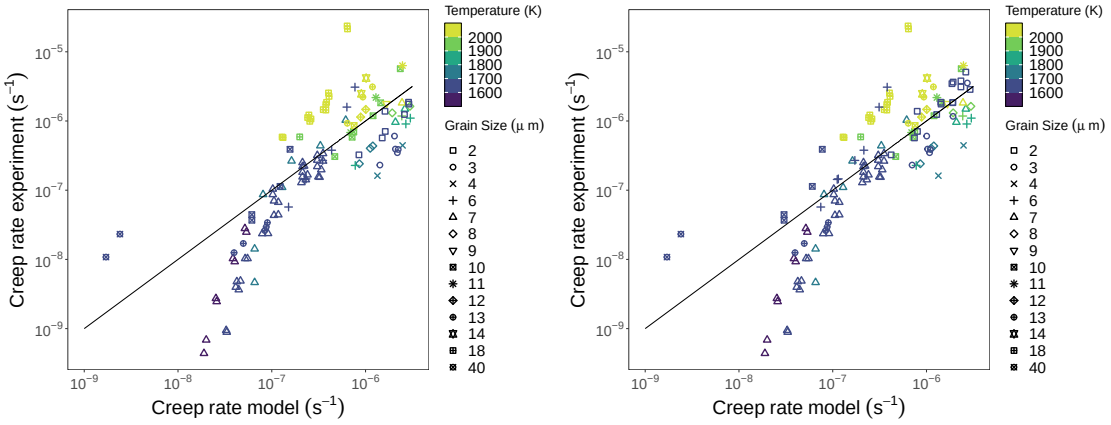

Figure 14: (a) Log-log plot of creep rate comparing experimental values with the model for the Σ9 grain boundary. The shapes represent different grain sizes and the color-bar represents the temperature. (b) Log-log plot of creep rate as a function of creep rate comparing experimental values with the model for the Σ11 grain boundary. The shapes represent different grain sizes and the color-bar represents the temperature

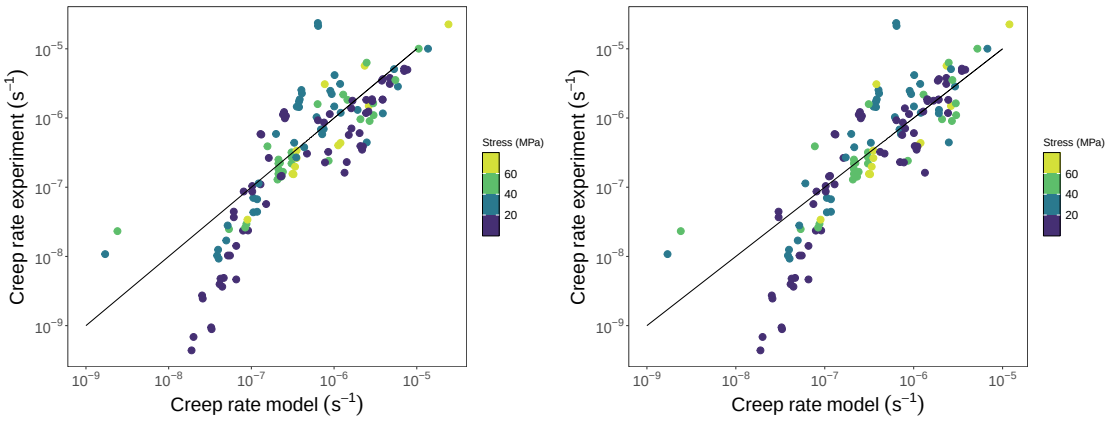

Figure 15: Log-log plot of creep rate comparing experimental values with the model for the Σ9 grain boundary. The color-bar represents the stress. (b) Log plot of creep rate as a function of creep rate comparing experimental values with the model for the Σ11 grain boundary. The color-bar represents the stress.

In a recent manuscript by Dillon et al.[53, 54], they developed a fitted model for nucleation rate limited kinetics which described existing creep data reasonably well for a number of materials including UO_2. In particular, it captured creep rates for UO_2 at low stresses and at temperatures below 1700 K. Using the parameters from [53], we have applied the new term to our creep rates, given by:

$$\dot{\epsilon} = \frac{42|\Omega_{GB,x}|D_x^{GB}[x_{GB}]\pi\delta}{k_B T G^3}\sigma_v \left(\frac{\dot{N}^2}{\dot{N}^2 + \frac{1}{2}}\right) \tag{20}$$

where $\dot{N}$ is a normalized grain boundary dislocation nucleation rate. It is a term that accounts for the fact that local regions of stress (such as at triple junctions) are enhanced relative to the applied stress and that this enables nucleation of defects. Therefore, $\dot{N}$ contains stress, grain size, temperatures dependencies that are described in more detail in [53].

Using the creep data in figures 14a and 15a, we obtain new creep rates that are shown in figures 16a and 16b. It can be seen that after applying the new term which accounts for stress concentration effects at singular points in the microstructure that can facilitate grain boundary dislocation nucleation, the systematic deviation of the model at low stresses and low temperatures is no longer there (see figures 16a and 16b). We now get a better description of the parity plot for all cases with an even distribution of scatter. Most of the scatter now occurs for grain sizes less than 3µm where other processes may be occurring, such as grain boundary sliding. This will be investigated in future work.

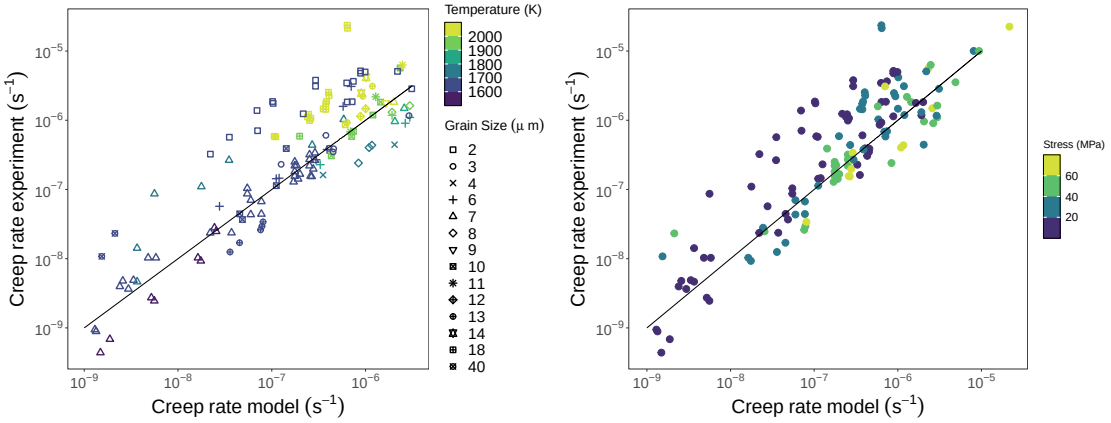

Figure 16: (a) Log-log plot of creep rate comparing experimental values with the model including the dislocation nucleation term for the Σ9 grain boundary. The shapes represent different grain sizes and the color-bar represents the temperature. (b)Log-log plot of creep rate comparing experimental values with the model dislocation nucleation term for the Σ9 grain boundary. The color-bar represents the stress.

3.5.3. Discussion

This study focuses on the uranium defect diffusion coefficient and concentrations at the grain boundary predicted using lower length-scale simulations. These properties underpin many processes in UO_2 and in this work we use the results to develop a mechanistic creep model in the diffusional regime.

As the uranium self-diffusion is important for many properties in UO_2 we have compared our results with experimental results, as shown in figure 8. Interestingly, there is a discrepancy between the different tracer experimental results. As Sabioni et al.[46] pointed out, many of the 'suggested' volume diffusion results were obtained from polycrystalline material and are actually more representative of results in the grain boundary. The true bulk behavior

is actually orders of magnitide lower, as shown by the single crystal tracer experiment done by Sabioni et al. [39] (orange solid line in figure 8) and by atomic scale simulations. While there are two grain boundary results (Alcock et al. [45] and Yajime et al. [44] shown by the open purple circles in figure 8) orders of magnitude higher than the grain boundary data by Sabioni et al. [46] (shown by green open circles), there is debate in the literature as to whether the data is representative, as discussed in [46]. They use the volume self diffusivity to calculate their grain boundary results and as we just discussed these values are higher than true bulk behavior.

If the uranium self diffusivity is backed out from experimental creep results assuming either Coble or Nabarro-Herring behavior, the values are orders of magnitude greater than the tracer experiments. However, our grain boundary uranium vacancy self-diffusion simulation results compare well against the results backed out from creep experiments assuming Coble behavior. Our bulk results match with the bulk tracer Sabioni et al. [39] data, which points to Coble being the dominant mechanism in the diffusional regime. This difference between the grain boundary tracer and Coble data suggest that the grain boundary tracer experiments in UO_2 should be revisited. We attribute the difference to the stoichiometry of the UO_2 when the experiments were carried out. It was shown in figure 9 that even small changes in stoichiometry (within the acceptable resolution of an experimental measurement) can vary the uranium self diffusion by orders of magnitude.

This simulation data was then fed into the mechanistic creep models (equations 1 and 2), along with the atomic volume at the grain boundary predicted from the elastic dipole tensor. We have a good agreement when compared to experimental data in the diffusional regime (see figures 10, 12, 13 and 14) and predict that the Coble creep mechanism is dominant - a point that is is still debated in literature [7, 9–21]. Moreover, when the non-stoichiometry dependence is examined (as shown in figure 12) there is a clear stoichiometry dependence for the Nabarro-Herring and the Coble regimes (which appears to be grain boundary dependent). However, in all the stoichiometry cases the Coble mechanism is dominant.

A recent paper by Dillon et al.[53, 54] has a term for stress concentration in the microstructure of UO_2 that can facilitate grain boundary dislocation nucleation. We applied this term to our creep model and significantly improved our parity plots (at low stresses) comparing creep rates predicted from our model to experiment, which show a good comparison over a range of stresses, grain sizes and temperatures.

4. Conclusions

A mechanistic diffusional creep model informed using lower length-scale simulations was developed for UO_2. In particular, we focus on the parameters that impact the Coble creep rate mechanism, namely; the uranium defect diffusion coefficient and concentration at the grain boundary. These parameters also underpin many other important phenomena in UO_2, such as fission gas release, void growth, grain growth and sintering. To calculate these we used MD to predict the diffusion coefficients at the grain boundary and developed a segregation energy model to predict the concentrations. We compared our uranium vacancy self-diffusion results with experimental results in literature and discussed where there is still some uncertainty. These values were then used in a mechanistic creep model, validated against experiment, and predicted that the Coble creep mechanism was dominant in the diffusional regime for UO_2. It is important to have a model to capture the correct mechanisms for creep in UO_2 as this can be

used as the foundation when applying to other fuels, such as doped UO_2, and when irradiation is accounted.

Acknowledgements

Funding for this work was provided by the US Department of Energy, Office of Nuclear Energy NEAMS (Nuclear Energy Advanced Modeling and Simulation) program. Los Alamos National Laboratory, an affirmative action/equal opportunity employer, is operated by Triad National Security, LLC, for the National Nuclear Security Administration of the U.S. Department of Energy under Contract No. 89233218CNA000001. This research used resources provided by the Los Alamos National Laboratory Institutional Computing Program, which is supported by the U.S. Department of Energy National Nuclear Security Administration under Contract No. 89233218CNA000001. This research made use of Idaho National Laboratory computing resources which are supported by the Office of Nuclear Energy of the U.S. Department of Energy and the Nuclear Science User Facilities under Contract No. DE-AC07-05ID14517.

References

[1] Thermophysical properties database of materials for light water reactors and heavy water reactors : final report of a coordinated research *Technical report*, June 2006

[2] ANP-10340NP Incorporation of chromia-doped fuel properties in AREVA approved methods.. *Technical report*, April, 2016.

[3] A. Massih. Effects of additives on uranium dioxide fuel behavior. Technical report, 2014.

[4] F. R. N. Nabarro. Deformation of Crystals by Motion of Single Ions. *Report on a Conference on the Strength of Solids*, 75, 1948.

[5] C. Herring. Diffusional Viscosity of a Polycrystalline Solid. *Journal of Applied Physics*, 21(5):437–445, may 1950.

[6] R. L. Coble. A Model for Boundary Diffusion Controlled Creep in Polycrystalline Materials. *Journal of Applied Physics*, 34(6):1679–1682, jun 1963.

[7] D. B. Knorr, R. M. Cannon, and R. L. Coble. Overview no. 84. *Acta Metallurgica*, 37(8):2103–2123, aug 1989.

[8] C. Matthews, R. Perriot, M. W. D. Cooper, C. R. Stanek, and D. A. Andersson. Cluster dynamics simulation of uranium self-diffusion during irradiation in UO_2. *Journal of Nuclear Materials*, 527:151787, 2019.

[9] P. E. Bohaboy, R. R. Asamoto, and A. E. Conti. Compressive Creep Characteristics of Stoichiometric Uranium Dioxide. *Other Information: UNCL. Orig. Receipt Date: 31-DEC-70*, (May), 1969.

[10] M. S. Seltzer, A. H. Clauer, and B. A. Wilcox. The stress dependence for high temperature creep of polycrystalline uranium dioxide. *Journal of Nuclear Materials*, 34(3):351–353, mar 1970.

[11] B. Burton, G. L. Reynolds, and J. P. Barnes. The influence of grain size on the creep of uranium dioxide. *Journal of Materials Science*, 8(12):1690–1694, dec 1973.

[12] B. Burton and G. L. Reynolds. The diffusional creep of uranium dioxide: its limitation by interfacial processes. *Acta Metallurgica*, 21(8):1073–1078, aug 1973.

[13] B. Burton and G. L. Reynolds. The influence of deviations from stoichiometric composition on the diffusional creep of uranium dioxide. *Acta Metallurgica*, 21(12):1641–1647, dec 1973.

[14] T. E. Chung and T. J. Davies. The superplastic creep of uranium dioxide. *Journal of Nuclear Materials*, 79(1):143–153, jan 1979.

[15] F. A. Mohamed and M. S. Soliman. On the creep behavior of uranium dioxide. *Materials Science and Engineering*, 53(2):185–190, may 1982.

[16] H. J. Frost and M. F. Ashby. Deformation-mechanism maps: the plasticity and creep of metals and ceramics. 1982.

[17] O. A. Ruano, J. Wolfenstine, J. Wadsworth, and O. D. Sherby. Harper-Dorn and power law creep in uranium dioxide. *Acta Metallurgica et Materialia*, 39(4):661–668, apr 1991.

[18] G. W. Greenwood. Denuded zones and diffusional creep. *Scripta Metallurgica et Materialia*, 30(12):1527–1530, jun 1994.

[19] B. Burton and G. L. Reynolds. In defense of diffusional creep. *Materials Science and Engineering: A*, 191(1-2):135–141, feb 1995.

[20] O. A. Ruano, O. D. Sherby, J. Wadsworth, and J. Wolfenstine. Rebuttal to In defense of diffusional creep . *Materials Science and Engineering: A*, 211(1-2):66–71, jun 1996.

[21] J. N. Wang and T. G. Nieh. A new interpretation of the mechanisms in Newtonian creep of uranium dioxides. *Journal of Nuclear Materials*, 228(1):141–147, feb 1996.

[22] M. R. Tonks, PC. A. Simon, and J. Hirschhorn. Mechanistic grain growth model for fresh and irradiated UO_2 nuclear fuel. *Journal of Nuclear Materials*, 543:152576, jan 2021.

[23] J. Spino, K. Vennix, and M. Coquerelle. Detailed characterisation of the rim microstructure in PWR fuels in the burn-up range 40 67 GWd/tM. *Journal of Nuclear Materials*, 231(3):179–190, aug 1996.

[24] V. V. Rondinella and T. Wiss. The high burn-up structure in nuclear fuel. *Materials Today*, 13(12):24–32, dec 2010.

[25] J. Rest, M. W. D. Cooper, J Spino, J.A. Turnbull, P. Van Uffelen, and C.T. Walker. Fission gas release from UO_2 nuclear fuel: A review. *Journal of Nuclear Materials*, 513:310–345, jan 2019.

[26] A. Goyal, S. R. Phillpot, G. Subramanian, D. A. Andersson, C. R. Stanek, and B. P. Uberuaga. Impact of homogeneous strain on uranium vacancy diffusion in uranium dioxide. *Physical Review B*, 91(9):094103, mar 2015.

[27] P. V. Nerikar, K. Rudman, T. G. Desai, D. Byler, C. Unal, K. J. McClellan, S. R. Phillpot, S. B. Sinnott, P. Peralta, B. P. Uberuaga, and C. R. Stanek. Grain Boundaries in Uranium Dioxide: Scanning Electron Microscopy Experiments and Atomistic Simulations. *Journal of the American Ceramic Society*, 94(6):1893–1900, jun 2011.

[28] E. Bourasseau, A. Mouret, P. F., Xavière Iltis, and R. C. Belin. Experimental and simulation study of grain boundaries in UO_2. *Journal of Nuclear Materials*, 517:286–295, apr 2019.

[29] Uberuaga B. P. and Andersson D. A. Uranium vacancy mobility at the $\Sigma 5$ symmetric tilt and $\Sigma 5$ twist grain boundaries in UO2. *Computational Materials Science*, 108, 80–87 2015

[30] M. W. D. Cooper, K. A. Gamble, L. Capolungo, C. Matthews, D. A. Andersson, B. Beeler, C.R. Stanek, and K. Metzger. Irradiation-enhanced diffusion and diffusion-limited creep in U_3Si_2. *Journal of Nuclear Materials*, 555:153129, nov 2021.

[31] A. P. Thompson, H. M. Aktulga, R. Berger, D. S. Bolintineanu, W. M. Brown, P. S. Crozier, Pieter J. in 't Veld, A. Kohlmeyer, S. G. Moore, T. D. Nguyen, R. Shan, M. J. Stevens, J. Tranchida, C. Trott, and S. J. Plimpton. LAMMPS - a flexible simulation tool for particle-based materials modeling at the atomic, meso, and continuum scales. *Computer Physics Communications*, 271:108171, feb 2022.

[32] M. W. D. Cooper, M. J. D. Rushton, and R. W. Grimes. A many-body potential approach to modelling the thermomechanical properties of actinide oxides. *Journal of Physics: Condensed Matter*, 26(10):105401, mar 2014.

[33] F. A. Kröger and H. J. Vink. Relations between the Concentrations of Imperfections in Crystalline Solids. In *Solid State Physics - Advances in Research and Applications*, volume 3, pages 307–435. 1956.

[34] X.-Y. Liu, M. W. D. Cooper, K. J. McClellan, J. C. Lashley, D. D. Byler, B. D. C. Bell, R. W. Grimes, C. R. Stanek, and D. A. Andersson. Molecular Dynamics Simulation of Thermal Transport in UO_2 Containing Uranium, Oxygen, and Fission-product Defects. *Physical Review Applied*, 6(4):044015, oct 2016.

[35] X.-Y. Liu, M. W. D. Cooper, K. J. McClellan, J. C. Lashley, D. D. Byler, B. D. C. Bell, R. W. Grimes, C. R. Stanek, and D. A. Andersson. Erratum: Molecular Dynamics Simulation of Thermal Transport in UO_2 Containing Uranium, Oxygen, and Fission-product Defects *Physical Review Applied*, 7(5):059901, may 2017.

[36] M. J. D. Rushton and A. Chroneos. Impact of uniaxial strain and doping on oxygen diffusion in CeO_2 . *Scientific Reports*, 4:2–7, aug 2014.

[37] R. D. Shannon. Revised effective ionic radii and systematic studies of interatomic distances in halides and chalcogenides. *Acta Crystallographica Section A*, 32(5):751–767, sep 1976.

[38] R. Perriot, C. Matthews, M. W.D. Cooper, B. P. Uberuaga, C. R. Stanek, and D. A. Andersson. Atomistic modeling of out-of-pile xenon diffusion by vacancy clusters in UO_2. *Journal of Nuclear Materials*, 520:96–109, jul 2019.

[39] A. C. S Sabioni, W. B. Ferraz, and F. Millot. First study of uranium self-diffusion in UO_2 by sims. *Journal of Nuclear Materials*, 257(2):180–184, 1998.

[40] Y. Ma. A study of point defects in $UO2 + x$ and their impact upon fuel properties. 2017.

[41] A. B. Auskern and J. Belle. Uranium ion self diffusion in UO_2. *Journal of Nuclear Materials*, 3(3):311–319, mar 1961.

[42] R. Lindner and F. Schmitz. Diffusion von Uran-233 in Urandioxyd. *Zeitschrift für Naturforschung A*, 16(12):1373–1378, dec 1961.

[43] H. Assmann and H. Stehle. Thermal and in-reactor densification of UO_2: Mechanisms and experimental results. *Nuclear Engineering and Design*, 48(1):49–67, jun 1978.

[44] S. Yajima, H. Furuya, and T. Hirai. Lattice and grain-boundary diffusion of uranium in UO_2. *Journal of Nuclear Materials*, 20(2):162–170, aug 1966.

[45] G. B. Alcock, R. J. Hawkins, A. W. D. Hills, and P. McNamara. *Paper SM-66/36, IAEA, Simp. Thermodynamics, Vienna*, 1965.

[46] A. C. S. Sabioni, W. B. Ferraz, and F. Millot. Effect of grain-boundaries on uranium and oxygen diffusion in polycrystalline UO_2. *Journal of Nuclear Materials*, 278(2-3):364–369, apr 2000.

[47] W. M. Armstrong, A. R. Causey, and W. R. Sturrock. Creep of single-crystal UO_2. *Journal of Nuclear Materials*, 19(1):42–49, apr 1966.

[48] W. G. Wolfer. Fundamental Properties of Defects in Metals. In *Comprehensive Nuclear Materials*, volume 1, pages 1–49. Elsevier, 2020.

[49] I. J. Fritz. Elastic properties of UO_2 at high pressure. *Journal of Applied Physics*, 47(10):4353–4358, oct 1976.

[50] M. S. Seltzer, A. H. Clauer, and B. A. Wilcox. The influence of stoichiometry on compression creep of polycrystalline UO_{2+x}. *Journal of Nuclear Materials*, 44(3):331–336, sep 1972.

[51] W. M. Armstrong, W.R. Irvine, and R. H. Martinson. Creep deformation of stoichiometric uranium dioxide. *Journal of Nuclear Materials*, 7(2):133–141, nov 1962.

[52] R. A. Wolfe and S. F. Kaufman. Machanical properties of oxide fulels LSBR/LWB DEVELOPMENT PROGRAM). No. WAPD-TM-587. Technical report, Bettis Atomic Power Lab., Pittsburgh, Pa.(US), 1967.

[53] S. J. Dillon, E. Lang, S. C. Finkeldei, J. Ouyang, and K. Hattar. A nucleation rate limited model for grain boundary creep. *Acta Materialia*, 246(December 2022):118718, mar 2023.

[54] M. F. Ashby On interface-reaction control of Nabarro-Herring creep and sintering. *Scripta Metallurgica*, 3(11):837–842 nov 1969.

Supplementary Information

1 V_U'''' Diffusion Calculations

The diffusivity of V_U'''' separated by grain boundary type for different charge compensation mechanisms is shown in figure 1. From this it is observed that the choice of charge mechanism used does not greatly impact the diffusivity.

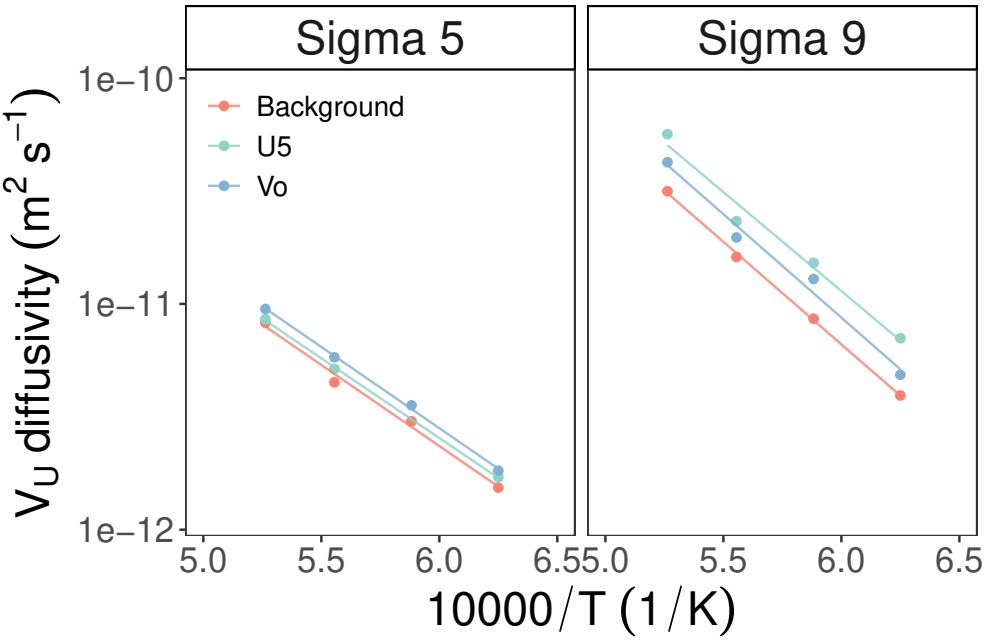

Figure 1

Figure 2: Arrhenius plot of uranium vacancy diffusion coefficient as a unction of inverse temperature for two grain boundary structures. The blue points are values for an oxygen charge compensation mechanism, the green points are values for a uranium^{5+} compensation mechanism and the red points represent a net background charge.

2 Segregation Energies

This section shows results of the segregation energies for V_U'''', $U_i^{\bullet\bullet\bullet\bullet}$, $V_O^{\bullet\bullet}$, $O_i^{\bullet\bullet}$, U_U' and $U_U^{\bullet}$ defects in the Σ9-(221) and Σ11-(1-13) tilt grain boundaries.

2.1 Σ9-(221)

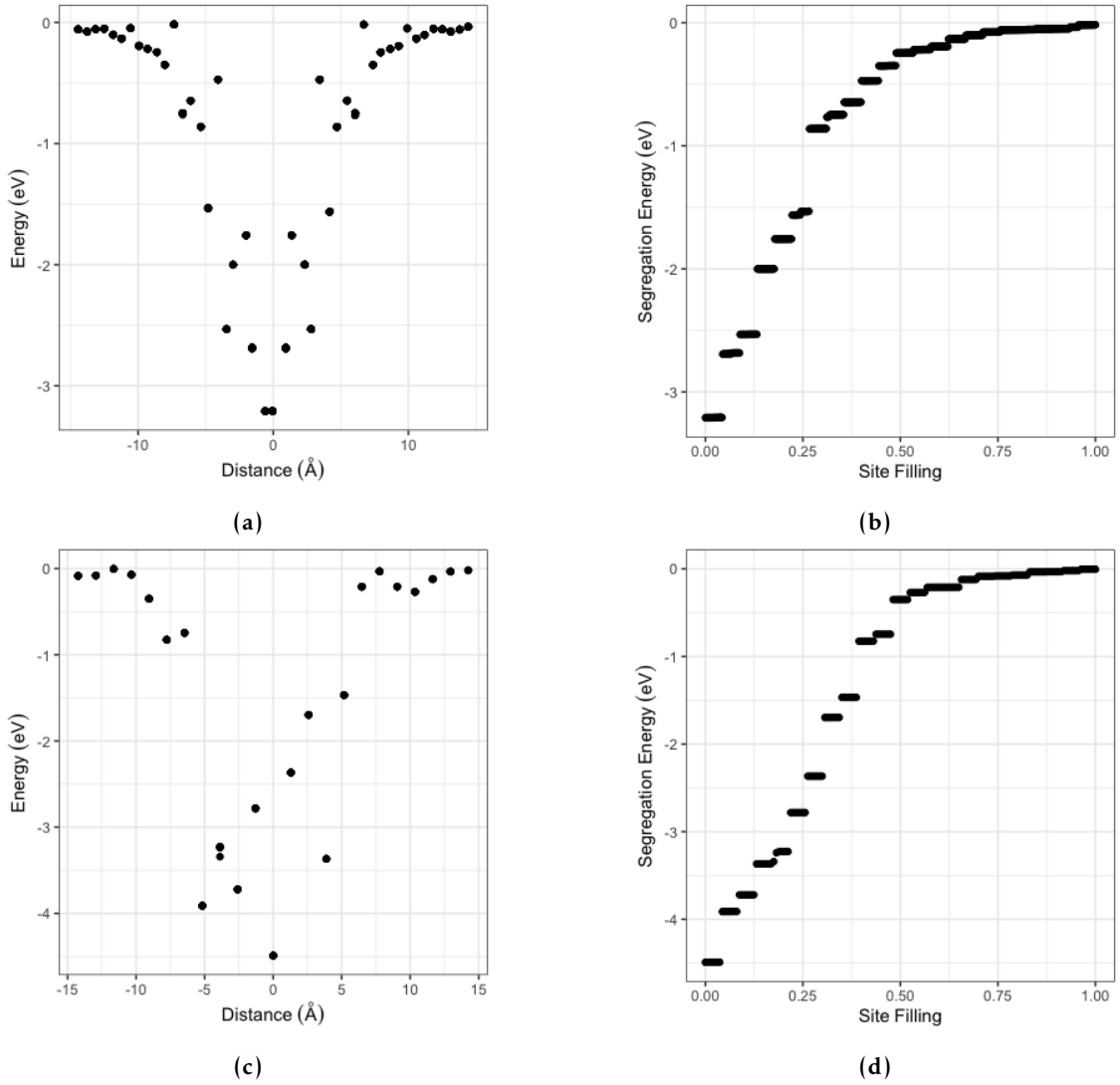

Figure 3: (a) V_U'''' segregation energy as a function of distance from grain boundary center denoted by 0. (b) V_U'''' segregation energy sorted by energy from lowest to highest. (c) $U_i^{\bullet\bullet\bullet\bullet}$ segregation energy as a function of distance from grain boundary center denoted by 0. (d) $U_i^{\bullet\bullet\bullet\bullet}$ segregation energy sorted by energy from lowest to highest.

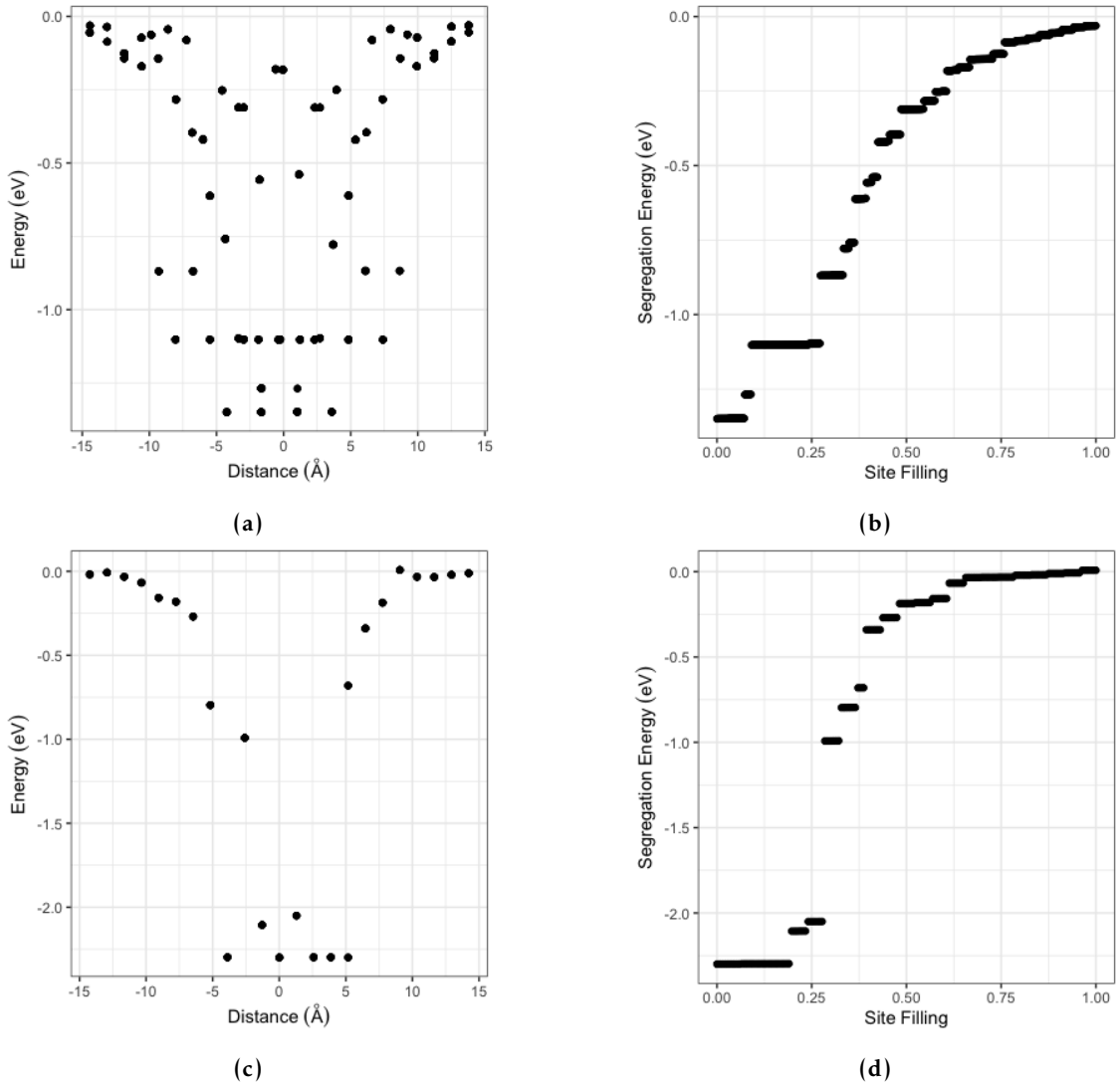

Figure 4: (a) V_O'''' segregation energy as a function of distance from grain boundary center denoted by 0. (b) V_O'''' segregation energy sorted by energy from lowest to highest. (c) $O_i^{\bullet\bullet\bullet\bullet}$ segregation energy as a function of distance from grain boundary center denoted by 0. (d) $O_i^{\bullet\bullet\bullet\bullet}$ segregation energy sorted by energy from lowest to highest.

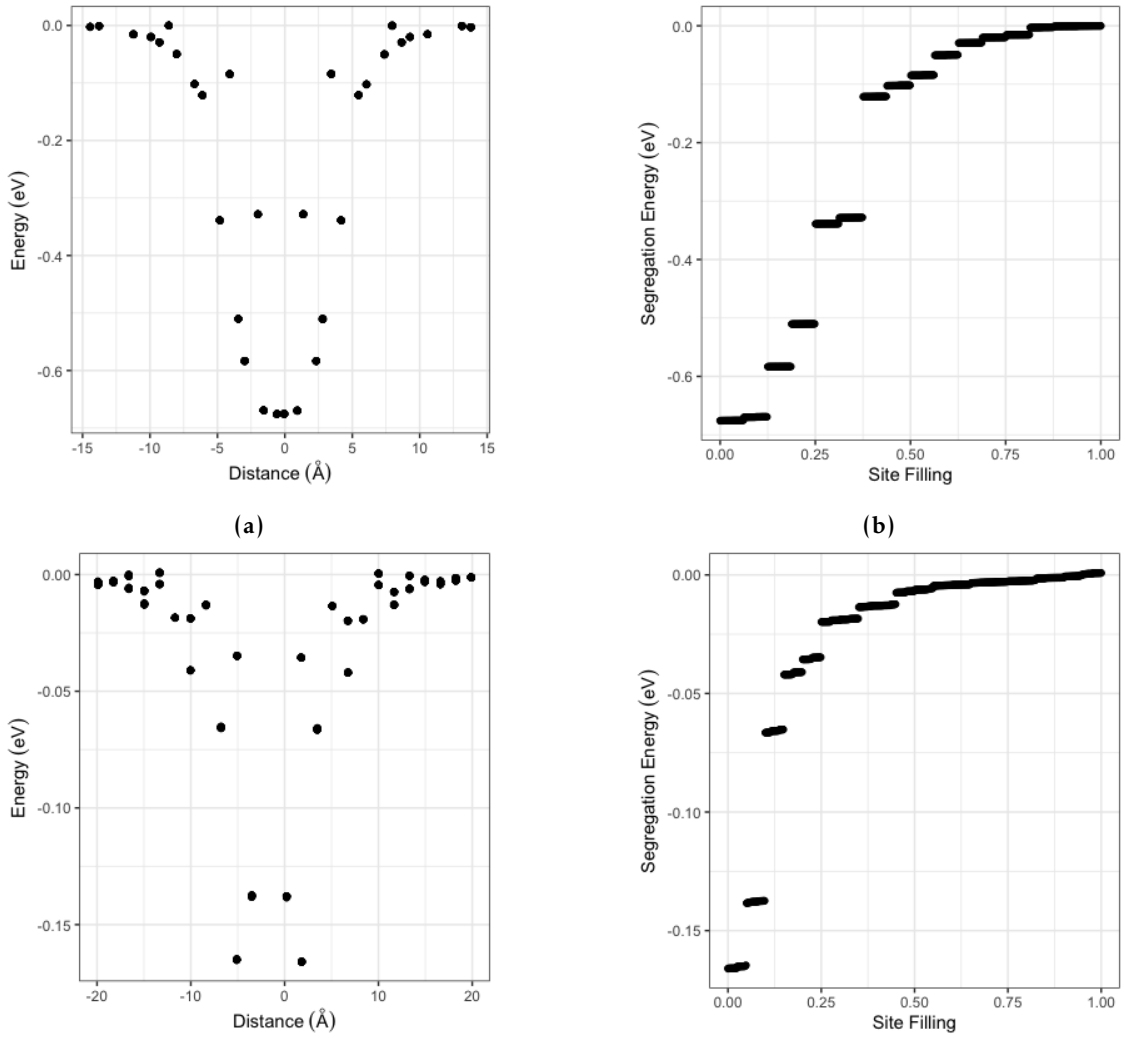

Figure 5: (a) U'_U segregation energy as a function of distance from grain boundary center denoted by 0. (b) U'_U segregation energy sorted by energy from lowest to highest. (c) $U^{\bullet}_U$ segregation energy as a function of distance from grain boundary center denoted by 0. (d) $U^{\bullet}_U$ segregation energy sorted by energy from lowest to highest.

2.2 Σ11-(1-13)

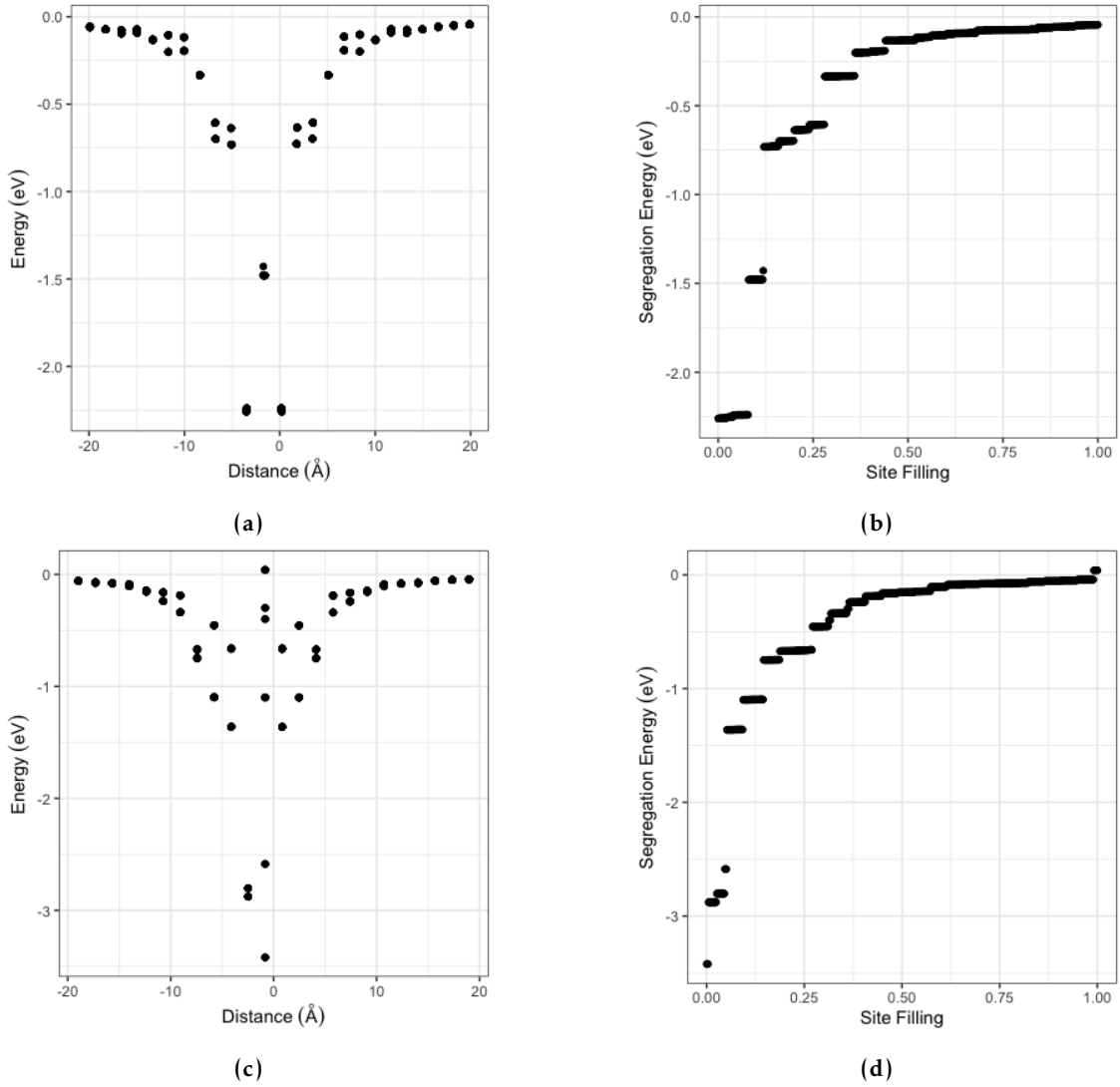

Figure 6: (a) V_U'''' segregation energy as a function of distance from grain boundary center denoted by 0. (b) V_U'''' segregation energy sorted by energy from lowest to highest. (c) $U_i^{\bullet\bullet\bullet\bullet}$ segregation energy as a function of distance from grain boundary center denoted by 0. (d) $U_i^{\bullet\bullet\bullet\bullet}$ segregation energy sorted by energy from lowest to highest.

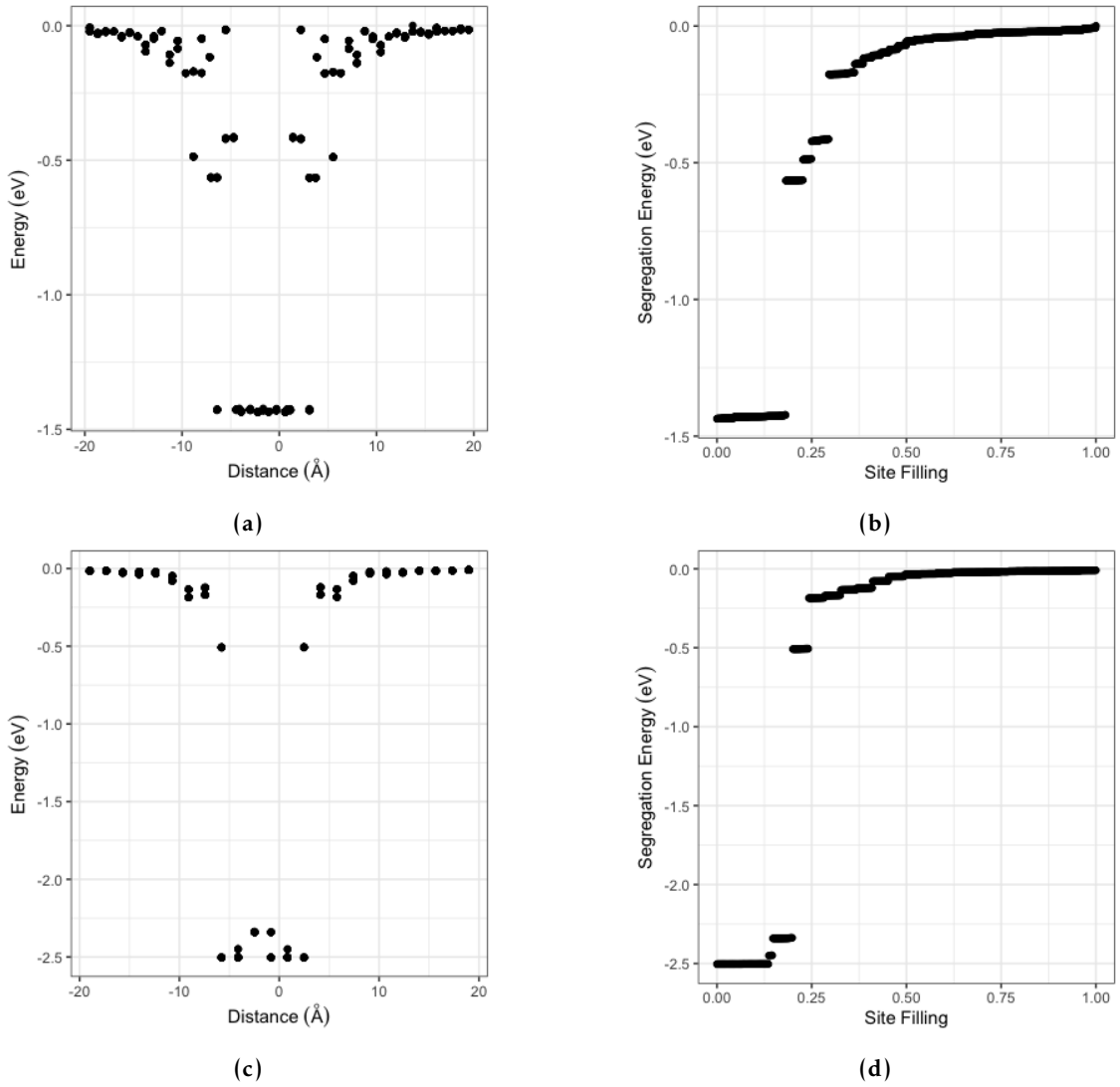

Figure 7: (a) V_O'''' segregation energy as a function of distance from grain boundary center denoted by 0. (b) V_O'''' segregation energy sorted by energy from lowest to highest. (c) $O_i^{\bullet\bullet\bullet\bullet}$ segregation energy as a function of distance from grain boundary center denoted by 0. (d) $O_i^{\bullet\bullet\bullet\bullet}$ segregation energy sorted by energy from lowest to highest.

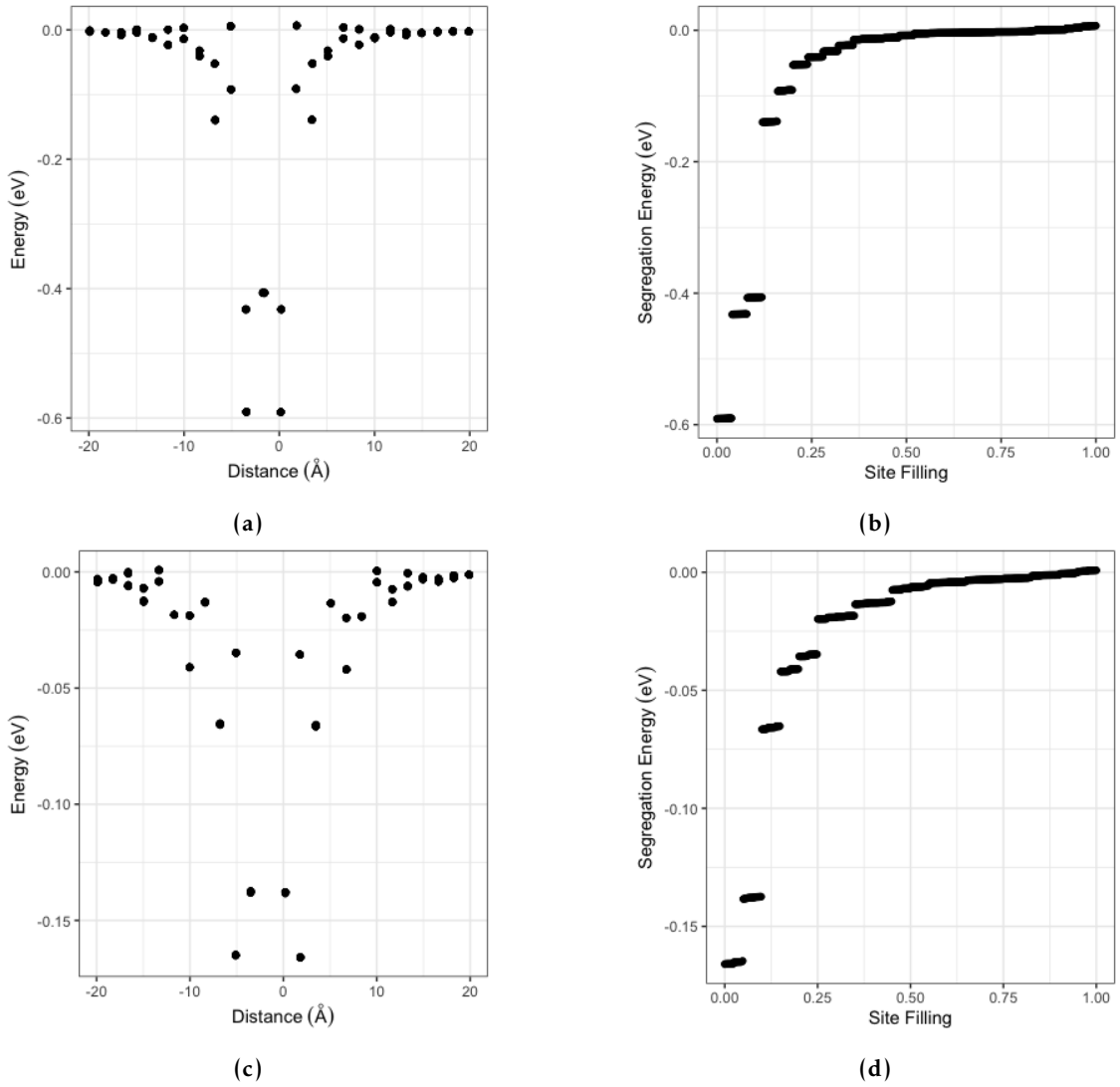

Figure 8: (a) U'_U segregation energy as a function of distance from grain boundary center denoted by 0. (b) U'_U segregation energy sorted by energy from lowest to highest. (c) $U^{\bullet}_U$ segregation energy as a function of distance from grain boundary center denoted by 0. (d) $U^{\bullet}_U$ segregation energy sorted by energy from lowest to highest.

3 Elastic Dipole Tensors

The energies in figures 9 and 10 are shown as a function of the reduced x position, where the x direction is normal to the grain boundary surface. The two grain boundaries are located at x=Lx = 0.5 and x=Lx = 0, which is equivalent to x=Lx = 1 due to the periodic boundaries.

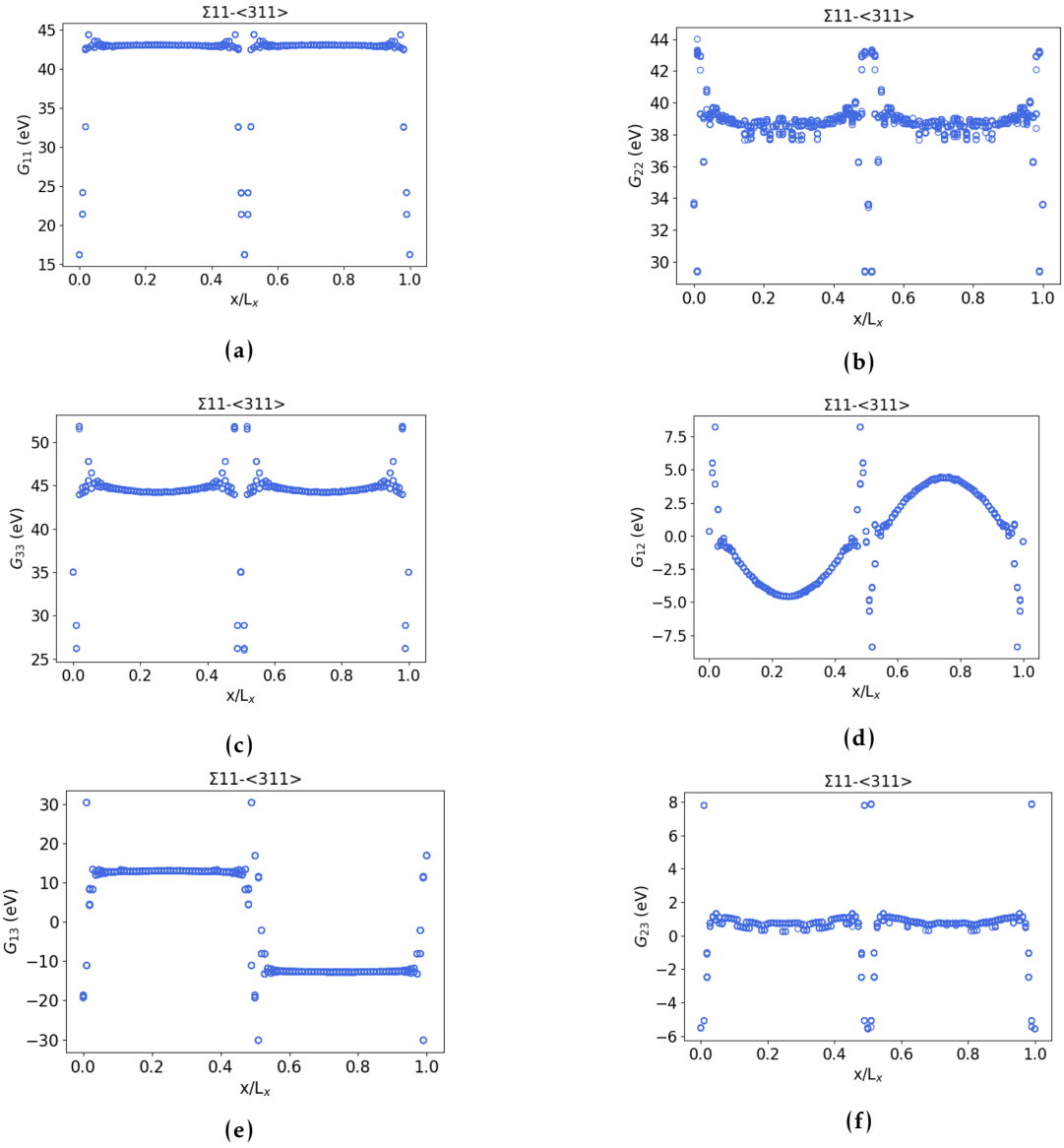

Figure 9: The elastic dipole tensor components for a V_U'''' corresponding to orthogonal and shear strains of the simulation supercell containing two Σ11-(311) GBs. The diagonal components $G_1 1$, $G_2 2$, and $G_3 3$ are shown in a), b), and c), respectively. The off-diagonal components $G_1 2$, $G_1 3$, and $G_2 3$ are shown in d), e), and f), respectively.

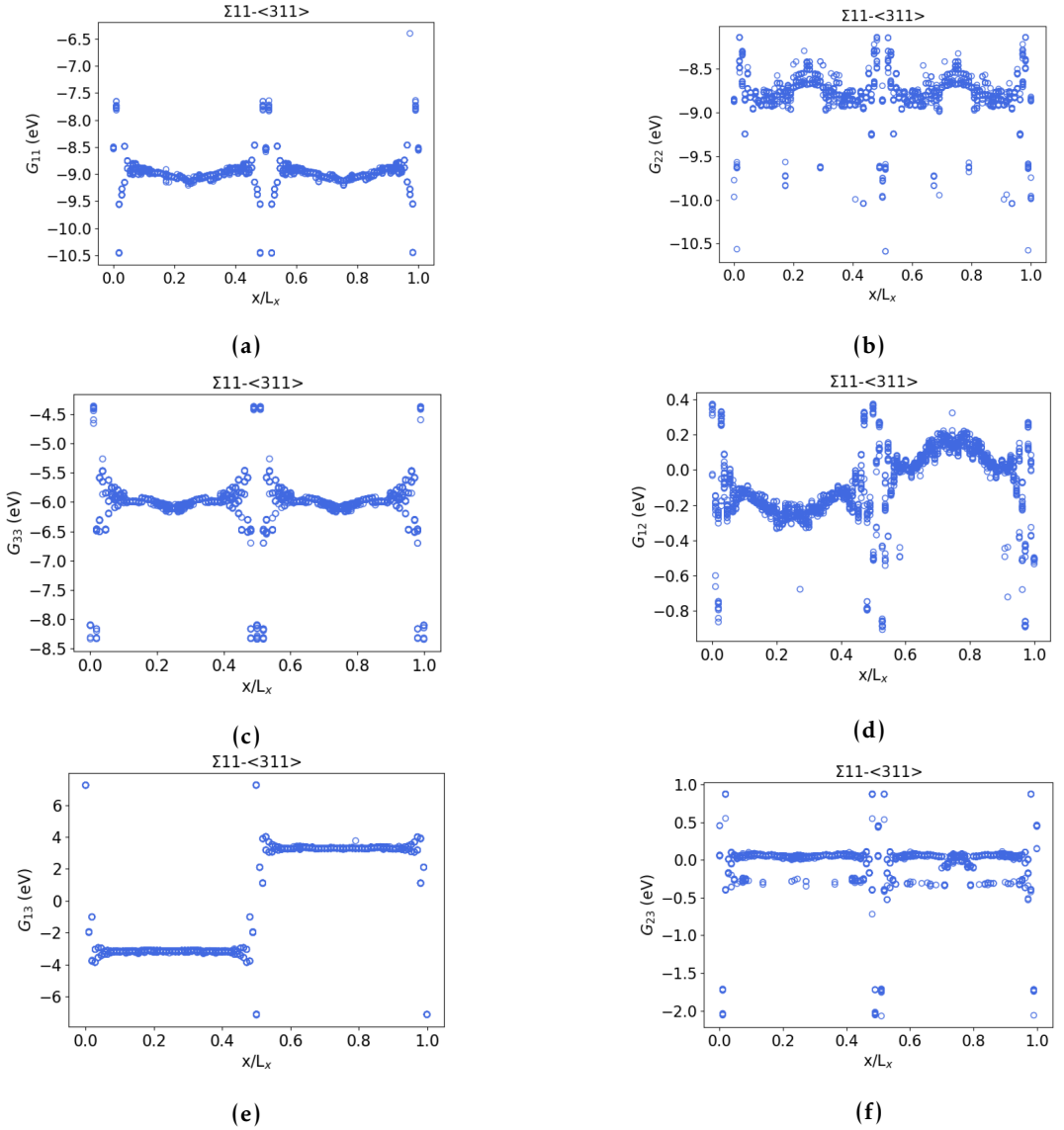

Figure 10: The elastic dipole tensor components for a $U_U^{\bullet}$ corresponding to orthogonal and shear strains of the simulation supercell containing two Σ11-(311) GBs. The diagonal components $G_1 1$, $G_2 2$, and $G_3 3$ are shown in a), b), and c), respectively. The off-diagonal components $G_1 2$, $G_1 3$, and $G_2 3$ are shown in d), e), and f), respectively.

4 Bulk Atomic Volumes

The atomic volumes for the bulk are presented in table 1 and only uranium vacancy defects that have a negative defect volume and are included, as these are the ones that influence creep.

Table 1: Uranium defect types and their corresponding absolute values of the atomic volumes.

Defect_x	$\lvert\Omega_x\rvert$ (m^3)
U_i	5.99009×10^{-29}
$U_i : 2O_i$	2.54003×10^{-29}
v_U	8.6013×10^{-30}
$v_U : v_O$	2.5991×10^{-30}
$v_U : 2v_O$	9.3579×10^{-30}
$2v_U : 2v_O$	4.8166×10^{-29}